

# TABLE OF CONTENTS

Abstract . . . . .	ii
<b>1 Introduction</b>	<b>2</b>
1.1 Research Statement . . . . .	2
1.2 Related Work . . . . .	5
1.2.1 GPUS for explicit and implicit methods . . . . .	5
1.2.2 GPUS/RBF . . . . .	5
1.2.3 RBF/Finite-Difference . . . . .	5
1.2.4 Preconditionners (info on that) . . . . .	5
1.2.5 Sparse matrix libraries . . . . .	5
1.2.6 Various GPU-based libraries . . . . .	5
1.2.7 Parallel implementations of RBF (there are any?) . . . . .	5
1.3 Fragments (integrate above) . . . . .	6
<b>2 The RBF-generated Finite Differences Method</b>	<b>8</b>
2.1 Background . . . . .	8
2.2 Stencil-based Derivative Approximation . . . . .	9
2.3 RBF-FD weights . . . . .	9
2.4 Weight Operators . . . . .	11
2.4.1 Laplacian ( $\nabla^2$ ) . . . . .	11
2.4.2 Laplace-Beltrami ( $\Delta_S$ ) on the Sphere . . . . .	11
2.4.3 Constrained Gradient ( $P_x \cdot \nabla$ ) on the Sphere . . . . .	12
2.5 Stabilization: Hyperviscosity . . . . .	13
2.6 Fragments (integrate above) . . . . .	13
<b>3 Parallel Solvers</b>	<b>17</b>
3.1 Distributed Solvers . . . . .	17
3.1.1 Node Partitioning . . . . .	17
3.1.2 Global and Local Indices . . . . .	17
3.1.3 Local Node Ordering . . . . .	17
3.2 Relation to the Restrictive Additive Schwarz Decomposition . . . . .	20
3.3 Overlapping Computation and Communication . . . . .	20
3.4 Parallel Linear Algebra Primitives . . . . .	22
3.5 Targeting the GPU . . . . .	22
3.5.1 Explicit Solvers . . . . .	22
3.5.2 Fragments (integrate above) . . . . .	26

3.5.3	Implicit Solvers . . . . .	26
<b>4</b>	<b>Numerical Validation</b>	<b>27</b>
4.1	Stencil Generation . . . . .	27
4.1.1	kD-Tree vs LSH . . . . .	27
4.2	Choosing $\epsilon$ . . . . .	27
4.3	Parabolic . . . . .	27
4.4	Hyperbolic . . . . .	27
4.4.1	Vortex Rollup . . . . .	28
4.4.2	Solid body rotation . . . . .	29
4.5	Fragments (integrate above) . . . . .	33
4.6	Elliptic . . . . .	34
<b>5</b>	<b>Performance Benchmarks</b>	<b>35</b>
5.1	OpenCL . . . . .	35
5.1.1	OpenCL vs CUDA . . . . .	35
5.1.2	Asynchronous Queuing . . . . .	36
5.2	Fermi Architecture . . . . .	36
5.2.1	Double Precision . . . . .	36
5.2.2	Local Caching . . . . .	36
5.2.3	Multiple Kernel Scheduling . . . . .	37
5.2.4	Future Nvidia Hardware . . . . .	37
5.3	HPC Spear Cluster . . . . .	37
5.4	Keeneland . . . . .	37
5.5	Future Hardware . . . . .	37
5.6	MPI_Alltoally . . . . .	37
5.7	Asynchronous OpenCL . . . . .	39
5.8	Multi-Queue OpenCL . . . . .	39
5.9	GPU Kernel Optimizations . . . . .	40
5.9.1	Work-Group Size and Number of Stencils . . . . .	40
5.9.2	Parallel Reduction in Shared Memory . . . . .	40
5.9.3	Comparison: custom SpMV for explicit schemes vs ViennaCL . . . . .	40
<b>6</b>	<b>Stokes</b>	<b>41</b>
6.1	Introduction . . . . .	41
6.2	RBF-FD Weights . . . . .	44
6.3	GPU Based Solver . . . . .	45
6.3.1	GMRES Algorithm . . . . .	45
6.3.2	Multiple GPUs . . . . .	45
6.4	Multiple GPUs . . . . .	46
6.4.1	Solution Ordering . . . . .	47
6.5	Governing Equations . . . . .	49
6.5.1	Constraints . . . . .	50
6.5.2	Manufactured Solution . . . . .	51
6.6	Preconditioning . . . . .	53

6.7	GMRES Results . . . . .	53
6.8	Fragments . . . . .	54
<b>7</b>	<b>Community Outreach</b>	<b>55</b>
<b>A</b>	<b>Avoiding Pole Singularities with RBF-FD</b>	<b>56</b>
<b>B</b>	<b>Projected Weights on the Sphere</b>	<b>58</b>
B.1	Direct Weights . . . . .	58
B.2	Indirect Weights . . . . .	59
B.3	Test Cases . . . . .	59
B.4	Conclusions . . . . .	60
	Bibliography . . . . .	64

# ABSTRACT

Many numerical methods based on Radial Basis Functions (RBFs) are gaining popularity in the geosciences due to their competitive accuracy, functionality on unstructured meshes, and natural extension into higher dimensions. One method in particular, the Radial Basis Function-generated Finite Differences (RBF-FD), has drawn significant attention due to its comparatively low computational complexity versus other RBF methods, high-order accuracy (6th to 10th order is common), and embarrassingly parallel nature.

Similar to classical Finite Differences, RBF-FD computes weighted differences of stencil node values to approximate derivatives at stencil centers. The method differs from classical FD in that the test functions used to calculate the differentiation weights are  $n$ -dimensional RBFs rather than one-dimensional polynomials. This allows for generalization to  $n$ -dimensional space on completely scattered node layouts.

We present our effort to capitalize on the parallelism within RBF-FD for geophysical flow. Many HPC systems around the world are transitioning toward significantly more Graphics Processing Unit (GPU) accelerators than CPUs. In addition to spanning multiple compute nodes, modern code design should include a second level of parallelism targeting the many-core GPU architectures. We will discuss our parallelization strategies to span computation across GPU clusters, and demonstrate the efficiency and accuracy of our parallel explicit and implicit solutions.

- what is new in the thesis (summarize: 1-2 pages)
- get all your figures
- 1/2 page description per figures
  - All figure captions (self-contained). Don't skimp on words.
- Previous work
  - GPUS/implicit methods
  - GPUS/RBF
  - RBF/Finite-Difference
  - Preconditionners (info on that)
  - Sparse matrix libraries
  - Various GPU/based libraries
  - Parallel implementations of RBF (there are any?)

Benchmarking....

- Timing (serial, parallel)
- Timing with special node reorderings. Explain logic

Test cases ...

Get all your references in bibtex. Send them to me.

Need detailed table of content.

Conditioning is defined as:

With condition number estimates we can choose a proper support parameter for uniformly distributed node sets.

Alternative algorithms exist for solving for RBF-FD weights when the systems are overly ill-conditioned. Currently, we have an unpublished algorithm ContourSVD available to play with (demonstrate accuracy improvements).

We make the assumption for now that we use regularly distributed nodes. Centroidal Voronoi tessellations provide reasonably good distributions for solutions. Examples (heat ellipse, ellipsoid, sphere, square cavity).

The motivation behind RBF-FD is generality/functionality in the numerical method. Scattered nodes are supported. Distribution requires proper choice of support, and tight nodes result in increased conditioning

# CHAPTER 1

## INTRODUCTION

### 1.1 Research Statement

What motivated this research?

The goal of this dissertation is to present a unified approach to parallel solutions of Partial Differential Equations (PDEs) with a method called Radial Basis Function-generated Finite Differences (RBF-FD).

**fix:** Many scientific problems of importance can be expressed as a collection of PDEs. Solutions to these problems provide answers to many simple questions such as the current temperature of a material, or perhaps the current position of a moving object. Complex and coupled PDEs can simulate the growth of zebra stripes or cheetah spots [37] or even model the flow of fluids. **Need refs for examples**

In order to solve these problems, computational numerical methods are employed on a discretized version of the domain. Traditionally, three **(and how would I classify FV? PartOfUnity?)** major categories exist for PDE solutions: finite difference (FD), finite element (FEM) and spectral element (SEM) [24]. Interestingly, all three of these methods rely on an underlying mesh, making them *meshed methods*. While each has had a turn in the spotlight, more recently a new category, or rather a generalization on all three previous categories, has emerged: *meshfree methods*.

The first task in traditional meshed methods is to generate an underlying grid/mesh. Node placement can be done in a variety of ways including uniform, non-uniform and random (monte carlo) sampling, or through iterative methods like Lloyd's algorithm that generate a regularized sampling of the domain (see e.g., [22]). **meshed methods have constraints on edge length and angle. Delaunay answers this, but is costly to compute Mesh2d, Triangle, DIstmesh** In addition to choosing nodes, meshed methods require connectivity/adjacency lists to form stencils (FD) or elements (FEM, SEM)—this implies an added challenge to cover the domain closure with a chosen element type. While these tasks may be straightforward in one- or two-dimensions, the extension into higher dimensions becomes increasingly more cumbersome [51].

Complex geometries, irregular boundaries and mesh refinement also pose a problem for meshed methods. As the complexity of the geometry/boundaries increases, so too should the resolution of the approximating mesh in order to accurately reconstruct the detail present. A naïve approach to refinement increases the density of nodes uniformly across the domain,

adding much more computation and memory storage than necessary for activity that is localized to sub-regions of the domain. Multiresolution methods attempt to compromise between accurate approximation of the domain and reduced resolution by one of two approaches: a) *multilevel methods* that decompose the model into a hierarchy with several levels of mesh detail, then only use a level when it is required to capture phenomena; and b) *adaptive irregular sampling* which has one level of detail, but non-uniform nodal density concentrated in areas of high activity [41]. Such techniques require robust methods and complex code capable of either coarsening/smoothing the approximate solutions to new level, or handling non-uniform node placement, element size etc.

Ideally, we seek a method defined on arbitrary geometries, that behaves regularly in any dimension, and avoids the cost of mesh generation. The ability to locally refine areas of interest in a practical fashion is also desirable. Fortunately, meshfree methods provide all of these properties: based wholly on a set of independent points in  $n$ -dimensional space, there is minimal cost for mesh generation, and refinement is as simple as adding new points where they are needed.

Since their adoption by the mathematics community in the 1980s ([24]), a plethora of meshfree methods have arisen for the solution of PDEs. For example, smoothed particle hydrodynamics, partition of unity method, element-free Galerkin method and others have been considered for fluid flow problems [15]. For a recent survey of methods see [51].

A subset of meshfree methods of particular interest to the community today revolves around Radial Basis Functions (RBFs). RBFs are a class of radially symmetric functions (i.e., symmetric about a point,  $x_j$ , called the *center*) of the form:

$$\phi_j(\mathbf{x}) = \phi(r(\mathbf{x})) \quad (1.1)$$

where the value of the univariate function  $\phi$  is a function of the Euclidean distance from the center point  $\mathbf{x}_j$  given by  $r(\mathbf{x}) = \|\mathbf{x} - \mathbf{x}_j\|_2 = \sqrt{(x - x_j)^2 + (y - y_j)^2 + (z - z_j)^2}$ . Examples of commonly used RBFs are available in Table ?? with their corresponding plots in Figure 1.1. RBF methods are based on a superposition of translates of these radially symmetric functions, providing a linearly independent but non-orthogonal basis used to interpolate between nodes in  $n$ -dimensional space. An example of RBF interpolation in 2D using 15 Gaussians is shown in Figure 1.2, where  $\phi_j(r(\mathbf{x}))$  is an RBF centered at  $\{\mathbf{x}_j\}_{j=1}^n$ .

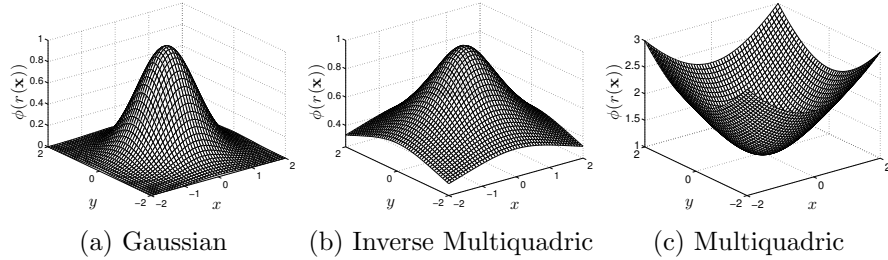


Figure 1.1: Commonly used RBFs.

With a history extending back four decades for RBF interpolation schemes [40], and two decades for RBFs applied to solving PDEs [45], many avenues of research remain untouched within their realm. Being a meshless method, RBF methods excel at solving problems that

require geometric flexibility with scattered node layouts in  $n$ -dimensional space. They naturally extend into higher dimensions without significant increase in programming complexity [28, 74]. In addition to competitive accuracy and convergence compared with other state-of-the-art methods [28, 29, 26, 74, 25], they also boast stability for large time steps.

Like most numerical methods, RBFs come with certain limitations. For example, RBF interpolation is—in general—not a well-posed problem, so it requires careful choice of positive definite or conditionally positive definite basis functions [41, 24]. The example 2D RBFs presented in Figure 1.1 are infinitely smooth and satisfy the (conditional) positive definite requirements.

Infinitely smooth RBFs depend on a shape or support parameter  $\epsilon$  that controls the width of the function. The functional form of the shape function becomes  $\phi(\epsilon r)$ . Decreasing  $\epsilon$  increases the support of the RBF and in most cases, the accuracy of the interpolation, but worsens the conditioning of the RBF interpolation problem [63]. The conditioning of the system also dramatically decreases as the number of nodes in the problem increases. Fortunately, recent algorithms such as Contour-Padé [31] and RBF-QR [35, 33] allow for numerically stable computation of interpolants in the nearly flat RBF regime (i.e.,  $\epsilon \rightarrow 0$ ) where high accuracy has been observed [50, 36].

Historically, the most common way to leverage RBFs for PDE solutions is in a global interpolation sense. That is, the value of a function value or any of its derivatives at a node location is a linear combination of all the function values over the *entire* domain, just as in a pseudospectral method. If using infinitely smooth RBFs, this leads to spectral (exponential) convergence of the RBF interpolant for smooth data [32]. As discussed in [29], global RBF methods require  $O(N^3)$  floating point operations (FLOPs) in pre-processing, where  $N$  is the total number of nodes, to assemble and solve a dense linear system for differentiation coefficients. The coefficients in turn are assembled into a dense Differentiation Matrix (DM) that is applied via matrix-vector multiply to compute derivatives at all  $N$  nodes for a cost of  $O(N^2)$  operations. assumes explicit scheme

Alternatively, one can use RBF-generated finite differences (RBF-FD) to introduce sparse DMs (Note: for pure interpolation, compactly supported RBFs can also introduce sparse matrices [72]). RBF-FD was first introduced by Tolstykh in 2000 [69], but it was the simultaneous, yet independent, efforts in [65], [68], [73] and [14] that gave the method its real start. RBF-FD share advantages with global RBF methods, like the ability to function without an underlying mesh, easily extend to higher dimensions and afford large time steps; however spectral accuracy is lost. Some of the advantages of RBF-FD include high computational speed together with high-order accuracy (6th to 10th order accuracy is common) and the opportunity for parallelization.

The RBF-FD method is similar in concept to classical finite-differences (FD): both methods approximate derivatives as a weighted sum of values at nodes within a nearby neighborhood. The two methods differ in that the underlying differentiation weights are exact for RBFs rather than polynomials.

As in FD, increasing the stencil size  $n$  increases the accuracy of the approximation. Given  $N$  total nodes in the domain (such as on the surface of a sphere),  $N$  linear systems, each of size  $n \times n$ , are solved to calculate the differentiation weights. Since  $n \ll N$ , the RBF-FD preprocessing complexity is dominated by  $O(N)$ —much lower than for the global RBF method of  $O(N^3)$ —with derivative evaluations on the order of  $O(nN) \implies O(N)$

FLOPs.

## 1.2 Related Work

- 1.2.1 GPUS for explicit and implicit methods
- 1.2.2 GPUS/RBF
- 1.2.3 RBF/Finite-Difference
- 1.2.4 Preconditionners (info on that)
- 1.2.5 Sparse matrix libraries
- 1.2.6 Various GPU/based libraries
- 1.2.7 Parallel implementations of RBF (there are any?)

RBF-FD have been successfully employed for a variety of problems including Hamilton-Jacobi equations [14], convection-diffusion problems [15, 67], incompressible Navier-Stokes equations [65, 16], transport on the sphere [34], and the shallow water equations [27].

As  $N$  grows larger, it behooves us to work on parallel architectures, be it CPUs or GPUs. With regard to the latter, there is some research on leveraging RBFs on GPUs in the fields of visualization [19, 71], surface reconstruction [18, 13], and neural networks [12]. However, research on the parallelization of RBF algorithms to solve PDEs on multiple CPU/GPU architectures is essentially non-existent. We have found three studies that have addressed this topic, none of which implement RBF-FD but rather take the avenue of domain decomposition for global RBFs (similar to a spectral element approach). In [21], Divo and Kassab introduce subdomains with artificial boundaries that are processed independently. Their implementation was designed for a 36 node cluster, but benchmarks and scalability tests are not provided. Kosec and Šarler [49] parallelize coupled heat transfer and fluid flow models using OpenMP on a single workstation with one dual-core processor. They achieved a speedup factor of 1.85x over serial execution, although there were no results from scaling tests. Yokota, Barba and Knepley [76] apply a restrictive additive Schwarz domain decomposition to parallelize global RBF interpolation of more than 50 million nodes on 1024 CPU processors. Only Schmidt et al. [64] have accelerated a global RBF method for PDEs on the GPU. Their MATLAB implementation applies global RBFs to solve the linearized shallow water equations utilizing the AccelerEyes Jacket [2] library to target a single GPU.

Within this dissertation, we have developed the first implementation of RBF-FD to span multiple CPUs. Each CPU has a corresponding GPU attached to it in a one-to-one correspondence. We thus also introduced the first known implementation of accelerated RBF-FD on the GPU.

continue with outline of chapters We present our explicit and implicit solutions to PDEs with our multi-GPU RBF-FD implementation.

$$\phi_j(\epsilon \|\mathbf{x} - \mathbf{x}_j\|) = e^{-(\epsilon \|\mathbf{x} - \mathbf{x}_j\|)^2}, (\epsilon = 2) \quad \hat{f}_N = \sum_{j=1}^N w_j \phi_j(\epsilon \|\mathbf{x} - \mathbf{x}_j\|)$$

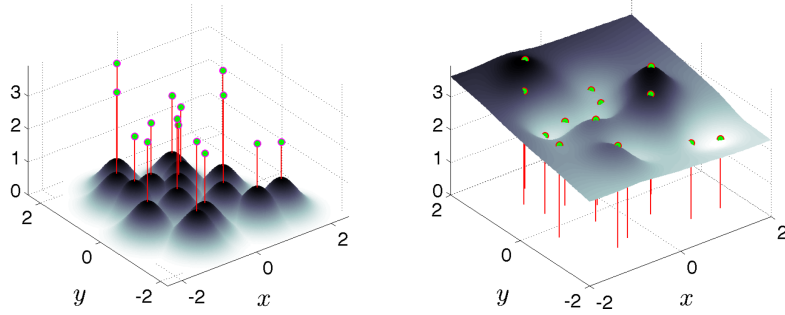


Figure 1.2: RBF interpolation using 15 translates of the Gaussian RBF with  $\epsilon = 2$ . One RBF is centered at each node in the domain. Linear combinations of these produce an interpolant over the domain passing through known function values.

### 1.3 Fragments (integrate above)

with the goal of solving coupled fluid flows modelling the physics (?) in the interior of the earth. We require both advective terms and diffusive terms. The components of a good pressure fluid solver are explicit and implicit differentiation. Whether we solve a steady-state PDE implicitly or a hyperbolic PDE with an implicit time-scheme, we require an *implicit solver*. An implicit solver is nothing but a method of assembling a differentiation matrix, forcing terms on the RHS and then solving the linear system. A direct LU factorization would suffice if our system is dense, but with RBF-FD the system is sparse. Sparse systems can be efficiently solved under the right conditions through sparse iterative solvers. :

Sufficient understanding of RBF interpolation led to the development of the first global RBF method for PDEs in [45]. Most popular among global methods is collocation, wherein RBF interpolation approximates the PDE solution by solving a large, dense linear system. In some cases RBF collocation demonstrates higher accuracy for the same number of nodes when compared to other state-of-the-art pseudospectral methods (e.g., [50] [?] [?]). In [?], spectral accuracy was demonstrated for hyperbolic PDEs even with local refinement of nodes in time.

Unfortunately—ill-conditioning aside—collocation methods are prohibitively expensive to solve when scaled to a large number of nodes. Assuming the collocation matrix does not change in time, global methods, with their dense systems, scale at  $O(N^3)$  operations for initial preconditioning/preprocessing followed by  $O(N^2)$  operations every time-step. This complexity is consistent with any collocation scheme. However, by introducing sparsity into the system (e.g., using compactly supported RBFs), the complexity is somewhat reduced.

General Purpose GPU (GPGPU) computing is one of today’s hottest trends within scientific computing. The release of NVidia’s CUDA at the end of 2006 marked both a redesign of GPU architecture, plus the addition of a new software layer that finally made GPGPU accessible to the general public. The CUDA API includes routines for memory control, interoperability with graphics contexts (i.e., OpenGL programs), and provides GPU implementation subsets of BLAS and FFTW libraries [55]. After the undeniable success of CUDA for C, new projects emerged to encourage GPU programming in languages like

FORTRAN (see e.g., HMPP [1] and Portland Group Inc.’s CUDA-FORTRAN [57]).

In early 2009, the Khronos Group—the group responsible for maintaining OpenGL—announced a new specification for a general parallel programming language referred to as the Open Compute Language (OpenCL) [48]. Similar in design to the CUDA language—in many ways it is a simple refactoring of the predecessor—the goal of OpenCL is to provide a mid-to-low level API and language to control any multi- or many-core processor in a uniform fashion. Today, OpenCL drivers exist for a variety of hardware including NVidia GPUs, AMD/ATI CPUs and GPUs, and Intel CPUs.

This *functional portability* is the cornerstone of the OpenCL language. However, functional portability does not imply performance portability. That is, OpenCL allows developers to write kernels capable of running on all types of target hardware, but optimizing kernels for one type of target (e.g., GPU) does not guarantee the kernel will run efficiently on another target (e.g., CPU). With CPUs tending toward many cores, and the once special purpose, many-core GPUs offering general purpose functionality, it is easy to see that soon the CPU and GPU will meet somewhere in the middle as general purpose many-core architectures. Already, ATI has introduced the Fusion APU (Accelerated Processing Unit) which couples an AMD CPU and ATI GPU within a single die. OpenCL is an attempt to standardize programming ahead of this intersection.

Petascale computing centers around the world are leveraging GPU accelerators to achieve peak performance. In fact, many of today’s high performance computing installations boast significantly more GPU accelerators than CPU counterparts. The Keeneland project is one such example, currently with 240 CPUs accompanied by 360 NVidia Fermi class GPUs with at least double that number expected by the end of 2012 [70].

Such throughput oriented architectures require developers to decompose problems into thousands of independent parallel tasks in order to fully harness the capabilities of the hardware. To this end, a plethora of research has been dedicated to researching algorithms in all fields of computational science. Of interest to us are methods for atmospheric- and geo-sciences.

# CHAPTER 2

## THE RBF-GENERATED FINITE DIFFERENCES METHOD

The process of solving PDEs using RBFs dates back to 1990 [45, 46]. This chapter starts with a description of the general approximation problem and provides background on RBF scattered data interpolation that will be required for the remainder of the chapter. This is followed by a description of Radial Basis Function-generated Finite Differences and examples of operators approximated by the method within this work.

We categorize existing methods for solving PDEs with RBFs as either global or local. Global methods use collocation and invert a single large linear system to find the interpolant that satisfies the differential equations at nodes in the domain. Local methods limit the influence of basis functions and seek an interpolant at each node defined in terms of neighboring basis functions (local collocation) or nodal values (RBF-FD). [Author's Note: list references of each type](#) [Author's Note: Do I need to define global collocation in the dissertation? The only purpose would be to compare complexity of RBF-FD with it](#)

### 2.1 Background

Consider a PDE expressed in terms of (linear) differential operators,  $\mathcal{L}$  and  $\mathcal{B}$ :

$$\begin{aligned}\mathcal{L}u &= f \quad \text{on } \Omega, \\ \mathcal{B}u &= g \quad \text{on } \Gamma\end{aligned}\tag{2.1}$$

where  $\Omega$  is the interior of the physical domain,  $\Gamma$  is the boundary of  $\Omega$  and  $f, g$  are known explicitly. In the case of a non-linear differential operator, a Newton's iteration, or some other method, can be used to linearize the problem (see e.g., [75]); of course, this increases the complexity of a single time step.

We solve PDEs of this form with *collocation*. That is, given a number of points in the domain, derivative and solution values are sought to best satisfy  $f, g$  at node locations. [Author's Note: Not clear yet. Review Lynch2005 for a better explanation\[?\]](#)

## 2.2 Stencil-based Derivative Approximation

The RBF-FD method is similar to classical Finite Differences in that differential quantities at a single node referred to as a *center*,  $\mathbf{x}_j$ , is approximated by weighted combinations of function values at  $n - 1$  neighboring nodes. The center node and its neighbors define a *stencil*,  $\{\mathbf{x}_i\}_{i=1}^n$ , in a localized (small) region or *neighborhood* of the domain.

Figure 2.1 provides two examples of RBF-FD stencils. First, Figure 2.1a illustrates a single stencil of size  $n = 13$  in a domain of randomly distributed nodes. The stencil center is represented by a green square, with the 12 neighboring nodes connected via red edges. The purple circle, the minimum covering circle for the stencil, demonstrates that the stencil contains only the 12 nearest neighbors of the center node. In Figure 2.1b, a larger RBF-FD stencil of size  $n = 75$  on the unit sphere is shown as red and blue disks surrounding the center represented as a square. Green disks are nodes outside of the stencil. The radii and color the red and blue disks represent the magnitude and sign of the RBF-FD weights determined to calculate a derivative quantity at the stencil center.

Weights for both classical Finite Difference and RBF-FD can be obtained through the solution of linear systems. In the case of Finite Difference, the system is a Vandermonde matrix. For RBF-FD the system is based on a symmetric distance matrix. [Author's Note: Need better description and ref:](#) The key difference between FD and RBF-FD systems is the singularity that occurs when two nodes swap.

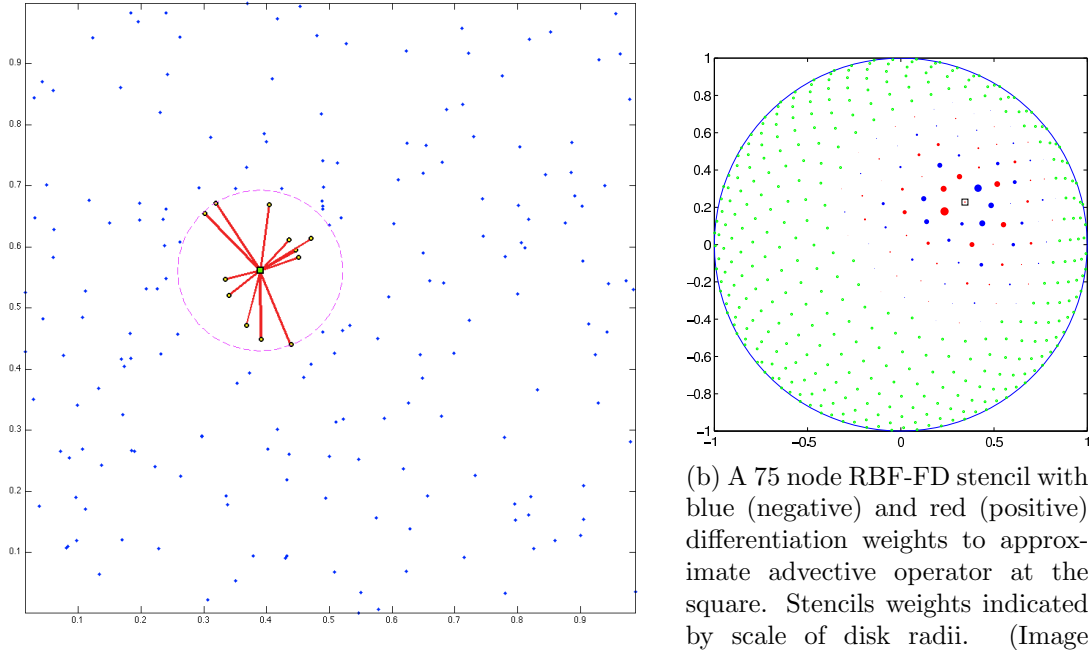
## 2.3 RBF-FD weights

Given a set of function values,  $\{u(\mathbf{x}_j)\}_{j=1}^N$ , on a set of  $N$  nodes  $\{\mathbf{x}_j\}_{j=1}^N$ , the operator  $\mathcal{L}$  acting on  $u(\mathbf{x})$  evaluated at  $\mathbf{x}_j$ , is approximated by a weighted combination of function values,  $\{u(\mathbf{x}_i)\}_{i=1}^n$ , in a small neighborhood of  $\mathbf{x}_j$ , where  $n \ll N$  defines the size of the stencil.

$$\mathcal{L}u(\mathbf{x})|_{\mathbf{x}=\mathbf{x}_j} \approx \sum_{i=1}^n w_i u(\mathbf{x}_i) + w_{n+1} p_0 \quad (2.2)$$

The RBF-FD weights,  $w_i$ , are found by enforcing that they are exact within the space spanned by the RBFs  $\phi_i(er) = \phi(\epsilon \|\mathbf{x} - \mathbf{x}_i\|)$ , centered at the nodes  $\{\mathbf{x}_i\}_{i=1}^n$ , with  $r = \|\mathbf{x} - \mathbf{x}_i\|$  being the distance between where the RBF is centered and where it is evaluated as measured in the standard Euclidean 2-norm. Various studies show [75, 30, 34, 27] that better accuracy is achieved when the interpolant can exactly reproduce a constant,  $p_0$ . Assuming  $p_0 = 1$ , the constraint  $\sum_{i=1}^n w_i = \mathcal{L}1|_{\mathbf{x}=\mathbf{x}_j} = 0$  completes the system:

$$\begin{pmatrix} \phi(\epsilon \|\mathbf{x}_1 - \mathbf{x}_1\|) & \phi(\epsilon \|\mathbf{x}_1 - \mathbf{x}_2\|) & \cdots & \phi(\epsilon \|\mathbf{x}_1 - \mathbf{x}_n\|) & 1 \\ \phi(\epsilon \|\mathbf{x}_2 - \mathbf{x}_1\|) & \phi(\epsilon \|\mathbf{x}_2 - \mathbf{x}_2\|) & \cdots & \phi(\epsilon \|\mathbf{x}_2 - \mathbf{x}_n\|) & 1 \\ \vdots & \ddots & \ddots & \vdots & \vdots \\ \phi(\epsilon \|\mathbf{x}_n - \mathbf{x}_1\|) & \phi(\epsilon \|\mathbf{x}_n - \mathbf{x}_2\|) & \cdots & \phi(\epsilon \|\mathbf{x}_n - \mathbf{x}_n\|) & 1 \\ 1 & 1 & \cdots & 1 & 0 \end{pmatrix} \begin{bmatrix} w_1 \\ w_2 \\ \vdots \\ w_n \\ w_{n+1} \end{bmatrix} = \begin{bmatrix} \mathcal{L}\phi(\epsilon \|\mathbf{x} - \mathbf{x}_1\|)|_{\mathbf{x}=\mathbf{x}_j} \\ \mathcal{L}\phi(\epsilon \|\mathbf{x} - \mathbf{x}_2\|)|_{\mathbf{x}=\mathbf{x}_j} \\ \vdots \\ \mathcal{L}\phi(\epsilon \|\mathbf{x} - \mathbf{x}_n\|)|_{\mathbf{x}=\mathbf{x}_j} \\ 0 \end{bmatrix}, \quad (2.3)$$



(a) A 13 node RBF-FD stencil of randomly distributed nodes. The stencil centered at the green square contains the 12 nearest neighbors contained within the minimum covering circle drawn in purple.

(b) A 75 node RBF-FD stencil with blue (negative) and red (positive) differentiation weights to approximate advective operator at the square. Stencils weights indicated by scale of disk radii. (Image courtesy of Bengt Fornberg and Natasha Flyer)

Figure 2.1: Examples of stencils computable with RBF-FD [Author's Note: Consider: show example FD stencil \(5pt with regular grid\)](#)

where  $w_{n+1}$  is ignored after the matrix in (2.3) is inverted. This  $n \times n$  system solve is repeated for each stencil center  $\mathbf{x}_j$ ,  $j = 1 \dots N$ , to form the  $N$  rows of the DM with  $n$  non-zeros ( $n \ll N$ ) per row. As an example, if  $\mathcal{L}$  is the identity operator, then the above procedure leads to RBF-FD interpolation. If  $\mathcal{L} = \frac{\partial}{\partial x}$ , one obtains the DM that approximates the first derivative in  $x$ . In the context of time-dependent PDEs, the stencil weights remain constant for all time-steps when the nodes are stationary. Therefore, the calculation of the differentiation weights is performed once in a single preprocessing step of  $O(n^3N)$  FLOPs. Improved efficiency is achieved by processing multiple right hand sides in one pass, calculating the weights corresponding to all required derivative quantities (i.e.,  $\frac{\partial}{\partial x}$ ,  $\frac{\partial}{\partial y}$ ,  $\nabla^2$ , etc.).

For each of the  $N$  small system solves of Equation (2.3), the  $n$  nearest neighbors to  $\mathbf{x}_j$  need to be located. This can be done efficiently using neighbor query algorithms or spatial partitioning data-structures such as Locality Sensitive Hashing (LSH) and  $k$ D-Tree. Different query algorithms often have a profound impact on the DM structure and memory access patterns. We choose a Raster ( $ijk$ ) ordering LSH algorithm [9] leading to the matrix structure in Figures 3.4 and 3.5. While querying neighbors for each stencil is an embarrassingly parallel operation, the node sets used here are stationary and require stencil generation only once. Efficiency and parallelism for this task has little impact on the overall run-time of tests, which is dominated by the time-stepping. We preprocess node sets and

generate stencils serially, then load stencils and nodes from disk at run-time. In contrast to the RBF-FD view of a static grid, Lagrangian/particle based PDE algorithms promote efficient parallel variants of LSH in order to accelerate querying neighbors at each time-step [56, 39].

## 2.4 Weight Operators

Throughout the development of our parallel code we have verified code correctness through the solution of a variety of PDEs. Here we provide a list of operators we have tested and their corresponding equations for the RHS of Equation 2.3 necessary to compute RBF-FD weights.

The standard first derivatives  $\frac{\partial}{\partial x}, \frac{\partial}{\partial y}, \frac{\partial}{\partial z}$ :

- $\frac{\partial \phi}{\partial x}$

where  $\frac{\partial \phi}{\partial r}$  for the Gaussian RBFs is given by:

### 2.4.1 Laplacian ( $\nabla^2$ )

2D:

3D:

### 2.4.2 Laplace-Beltrami ( $\Delta_S$ ) on the Sphere

The  $\nabla^2$  operator can be represented in spherical polar coordinates for  $\mathbb{R}^3$  as:

$$\nabla^2 = \underbrace{\frac{1}{r} \frac{\partial}{\partial r} \left( r^2 \frac{\partial}{\partial r} \right)}_{\text{radial}} + \underbrace{\frac{1}{r^2} \Delta_S}_{\text{angular}}, \quad (2.4)$$

where  $\Delta_S$  is the Laplace-Beltrami operator—i.e., the Laplacian operator constrained to the surface of the sphere. This form nicely illustrates the separation of components into radial and angular terms.

In the case of PDEs solved on the unit sphere, there is no radial term, so we have:

$$\nabla^2 \equiv \Delta_S. \quad (2.5)$$

Although this originated in the spherical coordinate system, [74] introduced the following Laplace-Beltrami operator for the surface of the sphere:

$$\Delta_S = \frac{1}{4} \left[ (4 - r^2) \frac{\partial^2}{\partial r^2} + \frac{4 - 3r^2}{r} \frac{\partial}{\partial r} \right], \quad (2.6)$$

where  $r$  is the Euclidean distance between nodes of an RBF-FD stencil and is independent of our choice of coordinate system.

### 2.4.3 Constrained Gradient ( $P_x \cdot \nabla$ ) on the Sphere

Additionally following [29, 27], the gradient operator must also be constrained to the sphere with this projection matrix:

$$P = I - \mathbf{x}\mathbf{x}^T = \begin{pmatrix} (1-x_1^2) & -x_1x_2 & -x_1x_3 \\ -x_1x_2 & (1-x_2^2) & -x_2x_3 \\ -x_1x_3 & -x_2x_3 & (1-x_3^2) \end{pmatrix} = \begin{pmatrix} P_{x_1} \\ P_{x_2} \\ P_{x_3} \end{pmatrix} \quad (2.7)$$

where  $\mathbf{x}$  is the unit normal at the stencil center.

The direct method of computing RBF-FD weights for the projected gradient for  $\mathbf{P} \cdot \nabla$  is presented in [29]. When solving for the weights, we apply the projection on the right hand side of our small linear system. We let  $\mathbf{x} = (x_1, x_2, x_3)$  be the stencil center, and  $\mathbf{x}_k = (x_{1,k}, x_{2,k}, x_{3,k})$  indicate an RBF-FD stencil node.

Using the chain rule, and assumption that

$$r(\mathbf{x}_k - \mathbf{x}) = \|\mathbf{x}_k - \mathbf{x}\| = \sqrt{(x_{1,k} - x_1)^2 + (x_{2,k} - x_2)^2 + (x_{3,k} - x_3)^2},$$

we obtain the unprojected gradient of  $\phi$  as

$$\nabla\phi(r(\mathbf{x}_k - \mathbf{x})) = \frac{\partial r}{\partial \mathbf{x}} \frac{\partial \phi(r(\mathbf{x}_k - \mathbf{x}))}{\partial r} = -(\mathbf{x}_k - \mathbf{x}) \frac{1}{r(\mathbf{x}_k - \mathbf{x})} \frac{\partial \phi(r(\mathbf{x}_k - \mathbf{x}))}{\partial r}$$

Applying the projection matrix gives

$$\begin{aligned} \mathbf{P}\nabla\phi(r(\mathbf{x}_k - \mathbf{x})) &= -(\mathbf{P} \cdot \mathbf{x}_k - \mathbf{P} \cdot \mathbf{x}) \frac{1}{r(\mathbf{x}_k - \mathbf{x})} \frac{\partial \phi(r(\mathbf{x}_k - \mathbf{x}))}{\partial r} \\ &= -(\mathbf{P} \cdot \mathbf{x}_k - 0) \frac{1}{r(\mathbf{x}_k - \mathbf{x})} \frac{\partial \phi(r(\mathbf{x}_k - \mathbf{x}))}{\partial r} \\ &= -(I - \mathbf{x}\mathbf{x}^T)(\mathbf{x}_k) \frac{1}{r(\mathbf{x}_k - \mathbf{x})} \frac{\partial \phi(r(\mathbf{x}_k - \mathbf{x}))}{\partial r} \\ &= \begin{pmatrix} x\mathbf{x}^T \mathbf{x}_k - x_k \\ y\mathbf{x}^T \mathbf{x}_k - y_k \\ z\mathbf{x}^T \mathbf{x}_k - z_k \end{pmatrix} \frac{1}{r(\mathbf{x}_k - \mathbf{x})} \frac{\partial \phi(r(\mathbf{x}_k - \mathbf{x}))}{\partial r} \end{aligned}$$

Thus, we directly compute the weights for  $P_x \cdot \nabla$  using these three RHS in Equation 2.3:

$$P \frac{\partial}{\partial x_1} = (x_1 \mathbf{x}^T \mathbf{x}_k - x_{1,k}) \frac{1}{r(\mathbf{x}_k - \mathbf{x})} \frac{\partial \phi(r(\mathbf{x}_k - \mathbf{x}))}{\partial r} \Big|_{\mathbf{x}=\mathbf{x}_j} \quad (2.8)$$

$$P \frac{\partial}{\partial x_2} = (x_2 \mathbf{x}^T \mathbf{x}_k - x_{2,k}) \frac{1}{r(\mathbf{x}_k - \mathbf{x})} \frac{\partial \phi(r(\mathbf{x}_k - \mathbf{x}))}{\partial r} \Big|_{\mathbf{x}=\mathbf{x}_j} \quad (2.9)$$

$$P \frac{\partial}{\partial x_3} = (x_3 \mathbf{x}^T \mathbf{x}_k - x_{3,k}) \frac{1}{r(\mathbf{x}_k - \mathbf{x})} \frac{\partial \phi(r(\mathbf{x}_k - \mathbf{x}))}{\partial r} \Big|_{\mathbf{x}=\mathbf{x}_j} \quad (2.10)$$

Alternatively, assuming weights for operators  $\nabla = \frac{\partial}{\partial x_1}, \frac{\partial}{\partial x_2}, \frac{\partial}{\partial x_3}$  are already computed, the projected operator could be constructed via weighting the unprojected gradient components. For example:

Author's Note: Show accuracy of derivative approximation when using projected operator vs linear combinations of dx,dy,dz operators

## 2.5 Stabilization: Hyperviscosity

For RBF-FD, differentiation matrices encode convective operators of the form

$$D = \alpha \frac{\partial}{\partial \lambda} + \beta \frac{\partial}{\partial \theta} \quad (2.11)$$

where  $\alpha$  and  $\beta$  are a function of the fluid velocity. The convective operator, discretized through RBF-FD, has eigenvalues in the right half-plane causing the method to be unstable [34, 27]. Stabilization of the RBF-FD method is achieved through the application of a hyperviscosity filter to Equation (2.11) [34]. By using Gaussian RBFs,  $\phi(r) = e^{-(\epsilon r)^2}$ , the hyperviscosity (a high order Laplacian operator) simplifies to

$$\Delta^k \phi(r) = \epsilon^{2k} p_k(r) \phi(r) \quad (2.12)$$

where  $k$  is the order of the Laplacian and  $p_k(r)$  are multiples of generalized Laguerre polynomials that are generated recursively (see [34]: Section 3.2). We assume a 2D Laplacian operator when working on the surface of the sphere since a local stencil can be viewed as lying on a plane.

In the case of parabolic and hyperbolic PDEs, hyperviscosity is added as a filter to the right hand side of the evaluation. For example, at the continuous level, the equation solved takes the form

$$\frac{\partial u}{\partial t} = -Du + Hu, \quad (2.13)$$

where  $D$  is the PDE operator, and  $H$  is the hyperviscosity filter operator. Applying hyperviscosity shifts all the eigenvalues of  $D$  to the left half of the complex plane. This shift is controlled by  $k$ , the order of the Laplacian, and a scaling parameter  $\gamma_c$ , defined by

$$H = \gamma \Delta^k = \gamma_c N^{-k} \Delta^k.$$

Given a choice of  $\epsilon$  (see Section 4.4.1), it was found experimentally that  $\gamma = \gamma_c N^{-k}$  provides stability and good accuracy for all values of  $N$  considered here. It also ensures that the viscosity vanishes as  $N \rightarrow \infty$  [27]. In general, the larger the stencil size, the higher the order of the Laplacian. This is attributed to the fact that, for convective operators, larger stencils treat a wider range of modes accurately. As a result, the hyperviscosity operator should preserve as much of that range as possible. The parameter  $\gamma_c$  must also be chosen with care and its sign depends on  $k$  (for  $k$  even,  $\gamma_c$  will be negative and for  $k$  odd, it will be positive). If  $\gamma_c$  is too large, the eigenvalues move outside the stability domain of our time-stepping scheme and/or eigenvalues corresponding to lower physical modes are not left intact, reducing the accuracy of our approximation. If  $\gamma_c$  is too small, eigenvalues remain in the right half-plane [34, 27].

## 2.6 Fragments (integrate above)

Global RBF collocation methods pose the problem of interpolating a multivariate function  $f : \Omega \rightarrow \mathbb{R}$  where  $\Omega \subset \mathbb{R}^m$ . Given a set of sample values  $\{f(x_j)\}_{j=1}^N$  on a discrete set of

nodes  $X = \{x_j\}_{j=1}^N \subset \Omega$ , an approximation  $\hat{f}_N$  can be constructed through linear combinations of interpolation functions. Here, we choose univariate, radially symmetric functions based on Euclidean distance ( $\|\cdot\|$ ), and use translates  $\phi(x - x_j)$  of a single continuous real valued function  $\phi$  defined on  $\mathbb{R}$  and centered at  $x_j$ :

$$\phi(x) := \varphi(\|x\|).$$

Here,  $\varphi$  is a Radial Basis Function and  $\phi$  the associated kernel. For simplification  $\phi_j(x)$  refers to a kernel centered at  $x_j$ ; i.e.,  $\varphi(\|x - x_j\|)$ .

The interpolant  $\hat{f}_N(x)$  requires a linear combination of translates:

$$\hat{f}_N(x) = \sum_{j=1}^N c_j \phi_j(x)$$

with real coefficients  $\{c_j\}_{j=1}^N$ . Assuming the interpolant passes through known values of  $f$ ; i.e.,

$$\hat{f}_N(x_i) = f(x_i), \quad 1 \leq i \leq N,$$

allows one to solve for coefficients if the following linear system is uniquely solvable:

$$\sum_{j=1}^N c_j \phi_j(x_i) = f(x_i), \quad 1 \leq i \leq N.$$

This is true if the  $N \times N$  matrix  $\Phi$  produced by the linear system

$$\begin{pmatrix} \phi_1(x_1) & \phi_2(x_1) & \cdots & \phi_N(x_1) \\ \phi_1(x_2) & \phi_2(x_2) & \cdots & \phi_N(x_2) \\ \vdots & \ddots & \ddots & \vdots \\ \phi_1(x_N) & \phi_2(x_N) & \cdots & \phi_N(x_N) \end{pmatrix} \begin{bmatrix} c_1 \\ c_2 \\ \vdots \\ c_N \end{bmatrix} = \begin{bmatrix} f(x_1) \\ f(x_2) \\ \vdots \\ f(x_N) \end{bmatrix}$$

$$\Phi \vec{c} = \vec{f}$$

is nonsingular.

When choosing an appropriate basis function for interpolation, a subset of RBFs have been shown to produce symmetric positive definite  $\Phi$ , while others are only conditionally positive definite (for more details see [24]). With the latter set, additional polynomial terms are added to constrain the system and enforce positive definiteness, resulting in this expanded system of equations:

$$\begin{aligned} \sum_{j=1}^N c_j \phi_j(x_i) + \sum_{k=1}^M d_k p_k(x_i) &= f(x_i), \quad 1 \leq i \leq N, \\ \sum_{j=1}^N c_j p_k(x_j) &= 0, \quad 1 \leq k \leq M. \end{aligned}$$

$$\begin{pmatrix} \Phi & P \\ P^T & 0 \end{pmatrix} \begin{bmatrix} c \\ d \end{bmatrix} = \begin{bmatrix} \vec{f} \\ 0 \end{bmatrix} \tag{2.14}$$

where  $\{p_k\}_{k=1}^M$  is a basis for  $\Pi_p^m$  (the set of polynomials in  $m$  variables of degree  $\leq p$ ) and

$$M = \binom{p+m}{m}.$$

Given the coefficients  $\vec{c}$ , the function value at a test point  $x$  is interpolated by

$$\begin{aligned}\hat{f}_N(x) &= \sum_{j=1}^N c_j \Phi_j(x) + \sum_{l=1}^M d_l P_l(x) \\ &= [\Phi \quad \mathbb{P}] \begin{bmatrix} c \\ d \end{bmatrix} \\ &= \vec{\Phi}_x^T \vec{c} \\ &= \vec{\Phi}_x^T \Phi^{-1} \vec{f}\end{aligned}\tag{2.15}$$

where  $\vec{c}$  is substituted by the solution to Equation 2.14. In Equation 2.15 the term  $\vec{\Phi}_x^T \Phi^{-1}$ , dependent only on node positions, can be evaluated prior to knowing  $f$ .

For the RBF-FD method, derivatives of  $u(x)$  are weighted combinations of a small neighborhood of  $N_s$  nodes (i.e., a stencil with  $N_s \ll N$ ):

$$\mathcal{L}u(x_1) \approx \sum_{j=1}^{N_s} c_j u(x_j)$$

where  $\mathcal{L}u$  denotes a linear differential quantity over  $u$  (e.g.,  $\mathcal{L}u = \frac{du}{dx}$ ). Here,  $c_j$  are unknown, and obtained by enforcing the reconstruction:

$$\mathcal{L}\phi_j(x_1) = \sum_{i=1}^{N_s} c_i \phi_j(x_i) \quad \text{for } j = 1, 2, \dots, N_s$$

with  $\mathcal{L}\phi_j$  provided by analytically applying the differential operator to the kernel function. This is equivalent to:

$$\begin{pmatrix} \phi_1(x_1) & \phi_1(x_2) & \cdots & \phi_1(x_{N_s}) \\ \phi_2(x_1) & \phi_2(x_2) & \cdots & \phi_2(x_{N_s}) \\ \vdots & \ddots & \ddots & \vdots \\ \phi_{N_s}(x_1) & \phi_{N_s}(x_2) & \cdots & \phi_{N_s}(x_{N_s}) \end{pmatrix} \begin{bmatrix} c_1 \\ c_2 \\ \vdots \\ c_{N_s} \end{bmatrix} = \begin{bmatrix} \mathcal{L}\phi_1(x_1) \\ \mathcal{L}\phi_2(x_1) \\ \vdots \\ \mathcal{L}\phi_{N_s}(x_1) \end{bmatrix} \tag{2.16}$$

$$\Phi_s \vec{c} = \vec{\Phi}_{\mathcal{L}_s}. \tag{2.17}$$

Solving Equation 2.17 for stencils weights,  $\vec{c}$ , and substituting into Equation 6.3 reveals the similarity between RBF-FD and the general problem of RBF interpolation (see Equation 2.15 and discussion):

$$\begin{aligned}\mathcal{L}u(x_1) &\approx (\Phi_s^{-1} \vec{\Phi}_{\mathcal{L}_s})^T \vec{u} \\ &\approx \vec{\Phi}_{\mathcal{L}_s}^T \Phi_s^{-T} \vec{u}\end{aligned}$$

Again, based on the choice of RBF, positive definiteness of the system is ensured by adding the same constraints as Equation 2.14, but note differential quantities for  $\vec{\mathbb{P}}$  on the right hand side:

$$\begin{pmatrix} \Phi_s & \mathbb{P} \\ \mathbb{P}^T & 0 \end{pmatrix} \begin{bmatrix} c \\ d \end{bmatrix} = \begin{bmatrix} \vec{\Phi}_{\mathcal{L}_s} \\ \vec{\mathbb{P}}_{\mathcal{L}} \end{bmatrix}. \quad (2.18)$$

Equation 2.18 is strictly for the stencil centered at node  $x_1$ . To obtain weights for all stencils in the domain, a total of  $N$  such systems must be solved.

Stabilization of the RBF-FD method is achieved through the application of a hyperviscosity filter [?]. By assuming the use of Gaussian RBFs,  $\phi(r) = e^{-(\epsilon r)^2}$ , the hyperviscosity operator simplifies to

$$\Delta^k \phi(r) = \epsilon^{2k} p_k(r) \phi(r). \quad (2.19)$$

The multiples of generalized Laguerre polynomials,  $p_k(r)$ , are obtained through the following recursive relation:

$$\begin{cases} p_0(r) = 1, \\ p_1(r) = 4(\epsilon r)^2 - 2d, \\ p_k(r) = 4((\epsilon r)^2 - 2(k-1) - \frac{d}{2})p_{k-1}(r) - 8(k-1)(2(k-1) - 2 + d)p_{k-2}(r), \quad k = 2, 3, \dots \end{cases}$$

where  $d$  is the dimension of the problem. We assume  $d = 2$  below when working on the surface of the sphere.

Many algorithms exist to query the  $k$ -nearest neighbors (equivalently all nodes in the minimum/smallest enclosing circle). Some algorithms overlay a grid similar to Locality Sensitive Hashing and query such as [?].

# CHAPTER 3

## PARALLEL SOLVERS

Parallelization of the RBF-FD method is achieved at two levels. First, the physical domain of the problem—in this case, the unit sphere—is partitioned into overlapping subdomains, each handled by a different CPU process. All CPUs operate independently to compute/load RBF-FD stencil weights, run diagnostic tests and perform other initialization tasks. A CPU computes only weights corresponding to stencils centered in the interior of its partition. After initialization, CPUs continue concurrently to solve the problem with explicit time-stepping. Communication barriers ensure that the CPUs execute in lockstep to maintain consistent solution values in regions where partitions overlap. The second level of parallelization offloads time-stepping of the PDE to the GPU. Evaluation of the right hand side of Equation (2.13) is data-parallel: the solution derivative at each stencil center is evaluated independently of the other stencils. This maps well to the GPU, offering decent speedup even in unoptimized kernels. Although the stencil weight calculation is also data-parallel, we assume that in this context that the weights are precomputed and loaded once from disk during the initialization phase.

Our current implementation assumes that we are computing on a cluster of CPUs, with one GPU attached to each CPU. The CPU maintains control of execution and launches kernels on the GPU that execute in parallel. Under the OpenCL standard [48], a tiered memory hierarchy is available on the GPU with *global device memory* as the primary and most abundant memory space. The memory space for GPU kernels is separate from the memory available to a CPU, so data must be explicitly copied to/from global device memory on the GPU.

### 3.1 Distributed Solvers

Need partitioning, global and local index maps, and local ordering for a distributed [61]

#### 3.1.1 Node Partitioning

#### 3.1.2 Global and Local Indices

#### 3.1.3 Local Node Ordering

After partitioning, each CPU/GPU is responsible for its own subset of nodes. To simplify accounting, we track nodes in two ways. Each node is assigned a global index, that uniquely

identifies it. This index follows the node and its associated data as it is shuffled between processors. In addition, it is important to treat the nodes on each CPU/GPU in an identical manner. Implementations on the GPU are more efficient when node indices are sequential. Therefore, we also assign a local index for the nodes on a given CPU, which run from 1 to the maximum number of nodes on that CPU.

It is convenient to break up the nodes on a given CPU into various sets according to whether they are sent to other processors, are retrieved from other processors, are permanently on the processor, etc. Note as well, that each node has a home processor since the RBF nodes are partitioned into multiple domains without overlap. Table 3.1, defines the collection of index lists that each CPU must maintain for both multi-CPU and multi-GPU implementations.

Figure 3.1 illustrates a configuration with two CPUs and two GPUs, and 9 stencils, four on CPU1, and five on CPU2, separated by a vertical line in the figure. Each stencil has size  $n = 5$ . In the top part of the figures, the stencils are laid out with blue arrows pointing to stencil neighbors and creating the edges of a directed adjacency graph. Note that the connection between two nodes is not always bidirectional. For example, node 6 is in the stencil of node 3, but node 3 is not a member of the stencil of node 6. Gray arrows point to stencil neighbors outside the small window and are not relevant to the following discussion, which focuses only on data flow between CPU1 and CPU2. Since each CPU is responsible for the derivative evaluation and solution updates for any stencil center, it is clear that some nodes have a stencil with nodes that are on a different CPU. For example, node 8 on CPU1 has a stencil comprised of nodes 4,5,6,9, and itself. The data associated with node 6 must be retrieved from CPU2. Similarly, the data from node 5 must be sent to CPU2 to complete calculations at the center of node 6.

The set of all nodes that a CPU interacts with is denoted by  $\mathcal{G}$ , which includes not only the nodes stored on the CPU, but the nodes required from other CPUs to complete the calculations. The set  $\mathcal{Q} \in \mathcal{G}$  contains the nodes at which the CPU will compute derivatives and apply solution updates. The set  $\mathcal{R} = \mathcal{G} \setminus \mathcal{Q}$  is formed from the set of nodes whose values must be retrieved from another CPU. For each CPU, the set  $\mathcal{O} \in \mathcal{Q}$  is sent to other CPUs. The set  $\mathcal{B} \in \mathcal{Q}$  consists of nodes that depend on values from  $\mathcal{R}$  in order to evaluate derivatives. Note that  $\mathcal{O}$  and  $\mathcal{B}$  can overlap, but differ in size, since the directed adjacency graph produced by stencil edges is not necessarily symmetric. The set  $\mathcal{B} \setminus \mathcal{O}$  represents nodes that depend on  $\mathcal{R}$  but are not sent to other CPUs, while  $\mathcal{Q} \setminus \mathcal{B}$  are nodes that have no dependency on information from other CPUs. The middle section Figure 3.1 lists global node indices contained in  $\mathcal{G}$  for each CPU. Global indices are paired with local indices to indicate the node ordering internal to each CPU. The structure of set  $\mathcal{G}$ ,

$$\mathcal{G} = \{\mathcal{Q} \setminus \mathcal{B}, \mathcal{B} \setminus \mathcal{O}, \mathcal{O}, \mathcal{R}\}, \quad (3.1)$$

is designed to simplify both CPU-CPU and CPU-GPU memory transfers by grouping nodes of similar type. The color of the global and local indices in the figure indicate the sets to which they belong. They are as follows: white represents  $\mathcal{Q} \setminus \mathcal{B}$ , yellow represents  $\mathcal{B} \setminus \mathcal{O}$ , green indices represent  $\mathcal{O}$ , and red represent  $\mathcal{R}$ .

The structure of  $\mathcal{G}$  offers two benefits: first, solution values in  $\mathcal{R}$  and  $\mathcal{O}$  are contiguous in memory and can be copied to or from the GPU without the filtering and/or re-ordering

---

$\mathcal{G}$	: all nodes received and contained on the CPU/GPU $g$
$\mathcal{Q}$	: stencil centers managed by $g$ (equivalently, stencils computed by $g$ )
$\mathcal{B}$	: stencil centers managed by $g$ that require nodes from another CPU/GPU
$\mathcal{O}$	: nodes managed by $g$ that are sent to other CPUs/GPUs
$\mathcal{R}$	: nodes required by $g$ that are managed by another CPU/GPU

---

Table 3.1: Sets defined for stencil distribution to multiple CPUs

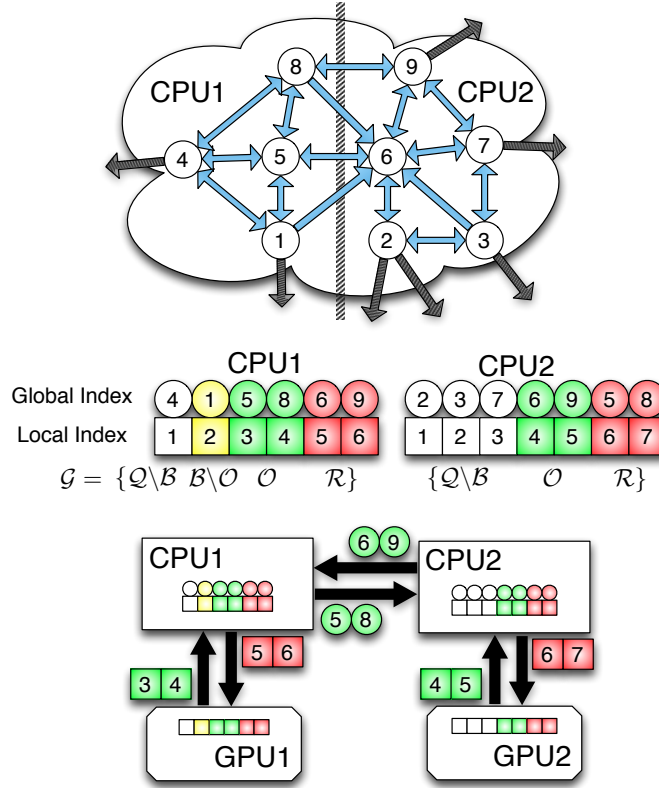


Figure 3.1: Partitioning, index mappings and memory transfers for nine stencils ( $n = 5$ ) spanning two CPUs and two GPUs. Top: the directed graph created by stencil edges is partitioned for two CPUs. Middle: the partitioned stencil centers are reordered locally by each CPU to keep values sent to/received from other CPUs contiguous in memory. Bottom: to synchronize GPUs, CPUs must act as intermediaries for communication and global to local index translation. Middle and Bottom: color coding on indices indicates membership in sets from Table 3.1:  $\mathcal{Q} \setminus \mathcal{B}$  is white,  $\mathcal{B} \setminus \mathcal{O}$  is yellow,  $\mathcal{O}$  is green and  $\mathcal{R}$  is red.

normally required in preparation for efficient data transfers. Second, asynchronous communication allows for the overlap of communication and computation. This will be considered as part of future research on algorithm optimization. Distinguishing the set  $\mathcal{B} \setminus \mathcal{O}$  allows the computation of  $\mathcal{Q} \setminus \mathcal{B}$  while waiting on  $\mathcal{R}$ .

When targeting the GPU, communication of solution or intermediate values is a four step process:

1. Transfer  $\mathcal{O}$  from GPU to CPU
2. Distribute  $\mathcal{O}$  to other CPUs, receive  $R$  from other CPUs
3. Transfer  $\mathcal{R}$  to the GPU
4. Launch a GPU kernel to operate on  $\mathcal{Q}$

The data transfers involved in this process are illustrated at the bottom of Figure 3.1. Each GPU operates on the local indices ordered according to Equation (3.1). The set  $\mathcal{O}$  is copied off the GPU and into CPU memory as one contiguous memory block. The CPU then maps local to global indices and transfers  $\mathcal{O}$  to other CPUs. CPUs send only the subset of node values from  $\mathcal{O}$  that is required by the destination processors, but it is important to note that node information might be sent to several destinations. As the set  $\mathcal{R}$  is received, the CPU converts back from global to local indices before copying a contiguous block of memory to the GPU.

This approach is scalable to a very large number of processors, since the individual processors do not require the full mapping between RBF nodes and CPUs.

Figure 3.2 illustrates a partitioning of  $N = 10,201$  nodes on the unit sphere onto four CPUs. Each partition, illustrated as a unique color, represents set  $\mathcal{G}$  for a single CPU. Alternating representations between node points and interpolated surfaces illustrates the overlap regions where nodes in sets  $\mathcal{O}$  and  $\mathcal{R}$  (i.e., nodes requiring MPI communication) reside. As stencil size increases, the width of the overlap regions relative to total number of nodes on the sphere also increases.

The linear partitioning in Figure 3.2 was chosen for ease of implementation. Communication is limited for each processor to left and right neighbors only, which simplifies parallel debugging. This partitioning, however, does not guarantee properly balanced computational work-loads. Other partitionings of the sphere exist but are not studied here because this paper's focus is neither on efficiency nor on selecting a partitioning strategy for maximum accuracy. Examples of alternative approaches include a cubed-sphere [42] or icosahedral geodesic grid [58], which can evenly balance the computational load across partitions. Other interesting partitionings can be generated with software libraries such as the METIS [47] family of algorithms, capable of partitioning and reordering directed graphs produced by RBF-FD stencils.

## 3.2 Relation to the Restrictive Additive Schwarz Decomposition

### 3.3 Overlapping Computation and Communication

Need to describe our approach to launch

In simplest form (& indicates an overlapped execution; overlapping is possible by non-blocking launches to the GPU before comm is started):

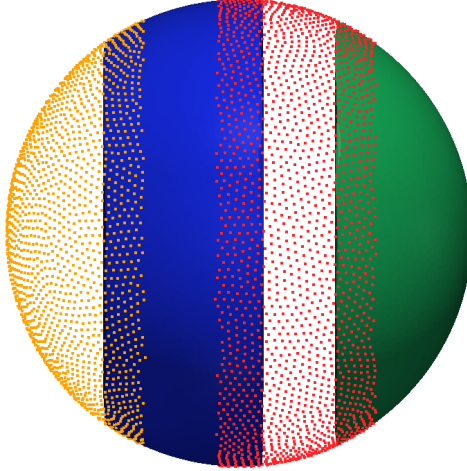


Figure 3.2: Partitioning of  $N = 10,201$  nodes to span four processors with stencil size  $n = 31$ .

- $U'_{Q \setminus B} = A_{Q \setminus B} U_{Q \setminus B}$
- & MPI\_alltoallv
- $U'_B = A_B U_B$

This form benefits because stencils are operated on in their entirety. For the GPU this is important because we maintain SIMD nature.

A more complex form which might overlap more comm and comp depending on the size of B (i.e., might be beneficial for large stencil sizes):

- $U'_{Q \setminus B} = A_{Q \setminus B} U_{Q \setminus B}$
- & MPI\_alltoallv
- &  $U'_B = A_{B \setminus R} U_{B \setminus R}$  (partial sparse vector product)
- $U'_B + = A_R U_R$

Note that there is no non-blocking version of MPI\_alltoallv within the MPI standard, so the above two algorithms will not be overlapped when computing on the CPU. To overlap on the CPU, [?] refers to the non-blocking collective as MPI\_ialltoallv. With a collective like this, we could enforce a pattern like:

- MPI\_alltoallv
- &  $U'_{Q \setminus B} = A_{Q \setminus B} U_{Q \setminus B}$
- &  $U'_B = A_{B \setminus R} U_{B \setminus R}$  (partial sparse vector product)
- MPI\_wait
- $U'_B + = A_R U_R$

## 3.4 Parallel Linear Algebra Primitives

The basic primitives necessary to parallelize our problems: SpMV, AXPY and

## 3.5 Targeting the GPU

### 3.5.1 Explicit Solvers

Our implementation leverages the GPU for acceleration of the standard fourth order Runge-Kutta (RK4) scheme. Nodes are stationary, so stencil weights are calculated once at the beginning of the simulation, and reused in every iteration. To avoid the cost of calculating stencil weights each time a test case is run, they are written to disk and loaded from file on subsequent runs. There is one set of weights computed for each new grid. Ignoring code initialization, the cost of the algorithm is simply the explicit time advancement of the solution.

Figure 3.3 summarizes the time advancement steps for the multi-CPU/GPU implementation. The RK4 steps are:

$$\begin{aligned}\mathbf{k}_1 &= \Delta t f(t_n, \mathbf{u}_n) \\ \mathbf{k}_2 &= \Delta t f\left(t_n + \frac{1}{2} \Delta t, \mathbf{u}_n + \frac{1}{2} \mathbf{k}_1\right) \\ \mathbf{k}_3 &= \Delta t f\left(t_n + \frac{1}{2} \Delta t, \mathbf{u}_n + \frac{1}{2} \mathbf{k}_2\right) \\ \mathbf{k}_4 &= \Delta t f(t_n + \Delta t, \mathbf{u}_n + \mathbf{k}_3) \\ \mathbf{u}_{n+1} &= \mathbf{u}_n + \frac{1}{6}(\mathbf{k}_1 + 2\mathbf{k}_2 + 2\mathbf{k}_3 + \mathbf{k}_4),\end{aligned}$$

where each equation has a corresponding kernel launch. To handle a variety of Runga-Kutta implementations, steps  $\mathbf{k}_{1 \rightarrow 4}$  correspond to calls to the same kernel with different arguments. The evaluation kernel returns two output vectors:

1.  $\mathbf{k}_i = \Delta t f(t_n + \alpha_i \Delta t, \mathbf{u}_n + \alpha_i \mathbf{k}_{i-1})$ , for steps  $i = 1, 2, 3, 4$ , and
2.  $\mathbf{u}_n + \alpha_{i+1} \mathbf{k}_i$

We choose  $\alpha_i = 0, \frac{1}{2}, \frac{1}{2}, 1, 0$  and  $\mathbf{k}_0 = \mathbf{u}_n$ . The second output for each  $\mathbf{k}_{i=1,2,3}$  serves as input to the next evaluation,  $\mathbf{k}_{i+1}$ . In an effort to avoid an extra kernel launch—and corresponding memory loads—the SAXPY that produces the second output uses the same evaluation kernel. Both outputs are stored in global device memory. When the computation spans multiple GPUs, steps  $\mathbf{k}_{1 \rightarrow 3}$  are each followed by a communication barrier to synchronize the subsets  $\mathcal{O}$  and  $\mathcal{R}$  of the second output (this includes copying the subsets between GPU and CPU). An additional synchronization occurs on the updated solution,  $\mathbf{u}_{n+1}$ , to ensure that all GPUs share a consistent view of the solution going into the next time-step.

To evaluate  $\mathbf{k}_{1 \rightarrow 4}$ , the discretized operators from Equation (2.13) are applied using sparse matrix-vector multiplication. If the operator  $D$  is composed of multiple derivatives, a differentiation matrix for each derivative is applied independently, including an additional multiplication for the discretized  $H$  operator. On the GPU, the kernel parallelizes across rows of the DMs, so all derivatives for stencils are computed in one kernel call.

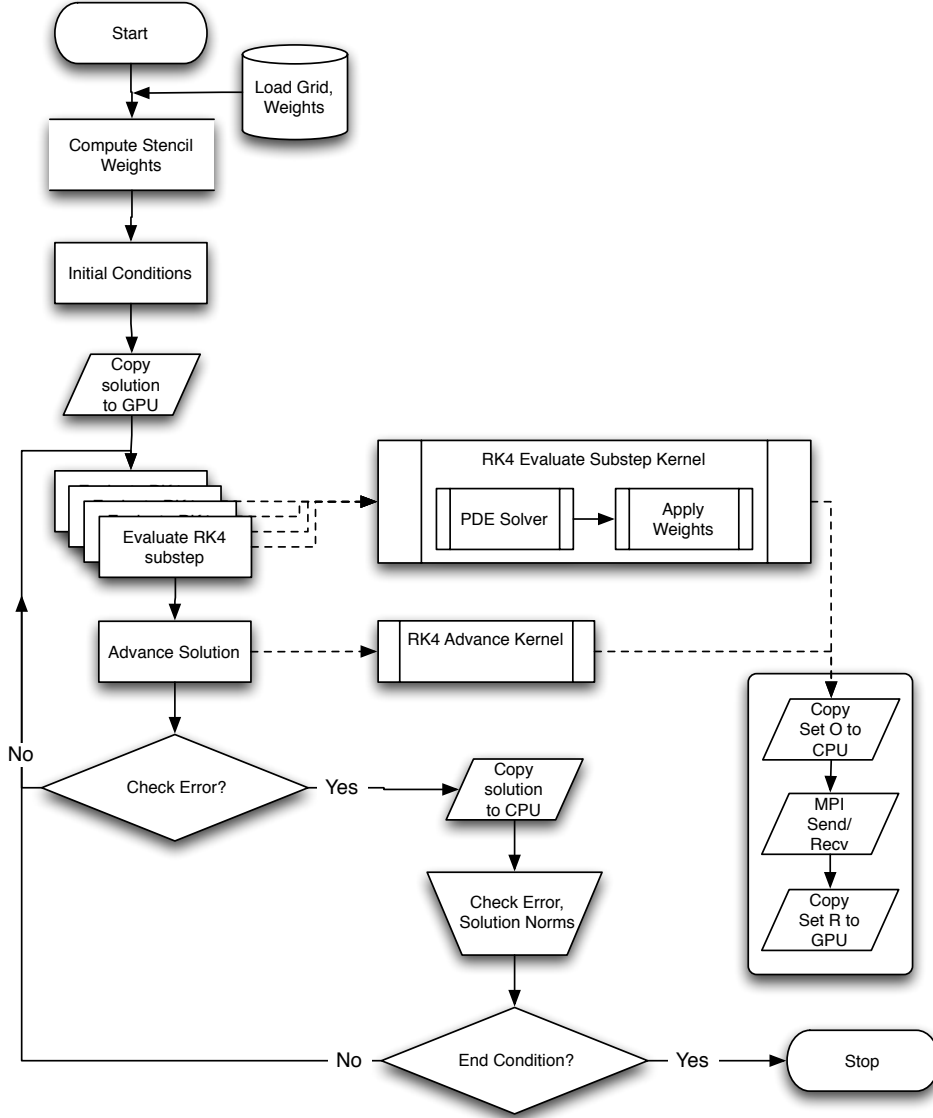


Figure 3.3: Workflow for RK4 on multiple GPUs.

For the GPU, the OpenCL language [48] assumes a lowest common denominator of hardware capabilities to provide functional portability. For example, all target architectures are assumed to support some level of SIMD (Single Instruction Multiple Data) execution for kernels. Multiple *work-items* execute a kernel in parallel. A collection of work-items performing the same task is called a *work-group*. While a user might think of work-groups as executing all work-items simultaneously, the work-items are divided at the hardware level into one or more SIMD *warps*, which are executed by a single multiprocessor. On the family of Fermi GPUs, a warp is 32 work-items [55]. OpenCL assumes a tiered memory hierarchy that provides fast but small *local memory* space that is shared within a work-group [48]. Local memory on Fermi GPUs is 48 KB per multiprocessor [55]. The *global device memory*

allows sharing between work-groups and is the slowest but most abundant memory. In the GPU computing literature, the terms *thread* and *shared memory* are synonymous to *work-item* and *local memory* respectively, and are preferred below.

Although the primary focus of this paper is the implementation and verification of the RBF-FD method across multiple CPUs and GPUs, we have nonetheless tested two approaches to the computation of derivatives on the GPU to assess the potential for further improvements in performance. In both cases, the stencil weights are stored in CSR format [4], a packed one-dimensional array in global memory with all the weights of a single stencil in consecutive memory addresses. Each operator is stored as an independent CSR matrix. The consecutive ordering on the weights implies that the solution vector, structured according to the ordering of set  $\mathcal{G}$  is treated as random access.

All the computation on the GPU is performed in 8-byte double precision.

**Naive Approach: One thread per stencil.** In this first implementation, each thread computes the derivative at one stencil center (Figure 3.4). The advantage of this approach is trivial concurrency. Since each stencil has the same number of neighbors, each derivative has an identical number of computations. As long as the number of stencils is a multiple of the warp size, there are no idle threads. Should the total number of stencils be less than a multiple of the warp size, the final warp would contain idle threads, but the impact on efficiency would be minimal assuming the stencil size is sufficiently large.

Perfect concurrency from a logical point of view does not imply perfect efficiency in practice. Unfortunately, the naive approach is memory bound. When threads access weights in global memory, a full warp accesses a 128-byte segment in a single memory operation [55]. Since each thread handles a single stencil, the various threads in a warp access data in very disparate areas of global memory, rather than the same segment. This leads to very large slowdowns as extra memory operations are added for each 128-byte segment that the threads of a warp must access. However, with stencils sharing many common nodes, and the Fermi hardware providing caching, some weights in the unused portions of the segments might remain in cache long enough to hide the cost of so many additional memory loads.

**Alternate Approach: One warp per stencil.** An alternate approach, illustrated in Figure 3.5, dedicates a full warp of threads to a single stencil. Here, 32 threads load the weights of a stencil and the corresponding elements of the solution vector. As the 32 threads each perform a subset of the dot product, their intermediate sums are accumulated in 32 elements of shared memory (one per thread). Should a stencil be larger than the warp size, the warp iterates over the stencil in increments of the warp size until the full dot product is complete. Finally, the first thread of the warp performs a sum reduction across the 32 (warp size) intermediate sums stored in shared memory and writes the derivative value to global memory.

By operating on a warp by warp basis, weights for a single stencil are loaded with a reduced number of memory accesses. Memory loads for the solution vector remain random access but see some benefit when solution values for a stencil are in a small neighborhood in the memory space. Proximity in memory can be controlled by node indexing (see e.g., [9] and [17]).

For stencil sizes smaller than 32, some threads in the warp always remain idle. Idle threads do not slow down the computation within a warp, but under-utilization of the GPU

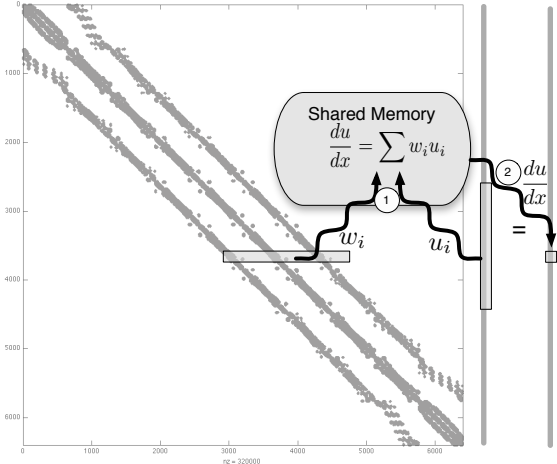


Figure 3.4: Naive approach to sparse matrix-vector multiply. Each thread is responsible for the sparse vector dot product of weights and solution values for derivatives at a single stencil.

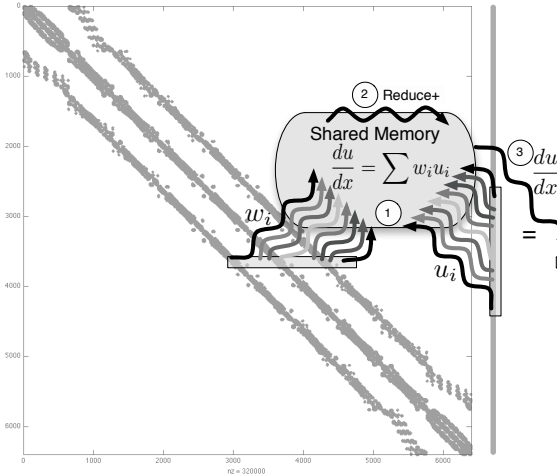


Figure 3.5: Alternative approach. A full warp (32 threads) collaborate to apply weights and compute the derivative at a stencil center.

is not desirable. For small stencil sizes, caching on the Fermi can hide some of the cost of memory loads for the naive approach, with no idle threads, making it more efficient. The real strength of one warp per stencil is seen for large stencil sizes. As part of future work on optimization, we will consider a parallel reduction in shared memory, as well as assigning multiple stencils to a single warp for small  $n$ .

### 3.5.2 Fragments (integrate above)

While the nomenclature used in this paper is typically associated with CUDA programming, the names *thread* and *warp* are used to clearly illustrate kernel execution in context of the NVidia specific hardware used in tests. OpenCL assumes a lowest common denominator of hardware capabilities to provide functional portability. However, intimate knowledge of hardware allows for better understanding of performance and optimization on a target architecture. For example, OpenCL assumes all target architectures are capable at some level of SIMD (Single Instruction Multiple Data) execution, but CUDA architectures allow for Single Instruction Multiple Thread (SIMT). SIMT is similar to traditional SIMD, but while SIMD immediately serializes on divergent operations, SIMT allows for a limited amount of divergence without serialization.

At the hardware level, a *thread* executes instructions on the GPU. On Fermi level GPUs, groups of 32 threads are referred to as *warps*. A warp is the unit of threads executed concurrently on a single *multi-processor*. In OpenCL (i.e., software), a collection of hardware threads performing the same instructions are referred to as a *work-group* of *work-items*. Work-groups execute as a collection of warps constrained to the same multiprocessor. Multiple work-groups of matching dimension are grouped into an *NDRRange*. The *kernel* provides a master set of instructions for all threads in an NDRRange [48].

NVidia GPUs have a tiered memory hierarchy related to the grouping of threads described above. In multiprocessors, each computing core executes a thread with a limited set of registers. The number of registers varies with the generation of hardware, but always come in small quantities (e.g., 32K shared by all threads of a multiprocessor on the Fermi). Accessing registers is free, but keeping data in registers requires an effort to maintain balance between kernel complexity and the number of threads per block. Threads of a single work-group can share information within a multiprocessor through *shared memory*. With only 48 KB available per multiprocessor [55], shared memory is another fast but limited resource on the GPU. OpenCL refers to shared memory as *local memory*. Sharing information across multiprocessors is possible in *global device memory*—the largest and slowest memory space on the GPU. To improve seek times into global memory, Fermi level architectures include L1 on each multiprocessor and a shared L2 cache for all multiprocessors.

### 3.5.3 Implicit Solvers

Perhaps this section should move up. I think it might be best to discuss GMRES and iterative methods before Distributed Solvers (that way we can say the general solution form is “matrix form”. but in parallel we need to use distributed algorithms.

# CHAPTER 4

## NUMERICAL VALIDATION

### 4.1 Stencil Generation

#### 4.1.1 kD-Tree vs LSH

#### 4.2 Choosing $\epsilon$

Present our attempts to get the right support parameter

### 4.3 Parabolic

Include figure tracking max temperature and min temperature. If we have zero flux conditions then they should average out. If we have Dirichlet BCs the temperature will converge to 0.

### 4.4 Hyperbolic

Here, we present the first results in the literature for parallelizing RBF-FDs on multi-CPU and multi-GPU architectures for solving PDEs. To verify our multi-CPU, single GPU and multi-GPU implementations, two hyperbolic PDEs on the surface of the sphere are tested: 1) vortex roll-up [54, 53] and 2) solid body rotation [43]. These tests were chosen since they are not only standard in the numerical literature, but also for the development of RBFs in solving PDEs on the sphere [28, 36, 26, 33]. Although any ‘approximately evenly’ distributed nodes on the sphere would suffice for our purposes, maximum determinant (MD) node distributions on the sphere are used (see [66] for details) in order to be consistent with previously published results (see e.g., [28] and [34]). Node sets from 1024 to 27,556 are considered with stencil sizes ranging from 17 to 101.

All results in this section are produced by the single-GPU implementation. Multi-CPU and multi-GPU implementations are verified to produce these same results. Synchronization of the solution at each time-step and the use of double precision on both the CPU and GPU ensure consistent results regardless of the number and/or choice of CPU vs GPU. Eigenvalues are computed on the CPU by the Armadillo library [62].

#### 4.4.1 Vortex Rollup

The first test case demonstrates vortex roll-up of a fluid on the surface of a unit sphere. An angular velocity field causes the initial condition to spin into two diametrically opposed but stationary vortices.

The governing PDE in latitude-longitude coordinates,  $(\theta, \lambda)$ , is

$$\frac{\partial h}{\partial t} + \frac{u}{\cos \theta} \frac{\partial h}{\partial \lambda} = 0 \quad (4.1)$$

where the velocity field,  $u$ , only depends on latitude and is given by

$$u = \omega(\theta) \cos \theta.$$

Note that the  $\cos \theta$  in  $u$  and  $1/\cos \theta$  in (4.1) cancel in the analytic formulation, so the discrete operator approximates  $\omega(\theta) \frac{\partial}{\partial \lambda}$ .

Here,  $\omega(\theta)$  is the angular velocity component given by

$$\omega(\theta) = \begin{cases} \frac{3\sqrt{3}}{2\rho(\theta)} \operatorname{sech}^2(\rho(\theta)) \tanh(\rho(\theta)) & \rho(\theta) \neq 0 \\ 0 & \rho(\theta) = 0 \end{cases}$$

where  $\rho(\theta) = \rho_0 \cos \theta$  is the radial distance of the vortex with  $\rho_0 = 3$ . The exact solution to (4.1) at non-dimensional time  $t$  is

$$h(\lambda, \theta, t) = 1 - \tanh\left(\frac{\rho(\theta)}{\gamma} \sin(\lambda - \omega(\theta)t)\right),$$

where  $\gamma$  defines the width of the frontal zone.

From a method of lines approach, the discretized version of (4.1) is

$$\frac{d\mathbf{h}}{dt} = -\operatorname{diag}(\omega(\theta)) D_\lambda \mathbf{h}. \quad (4.2)$$

where  $D_\lambda$  is the DM containing the RBF-FD weights that approximate  $\frac{\partial}{\partial \lambda}$  at each node on the sphere.

For stability, hyperviscosity is added to the right hand side of (4.2) in the form given in (2.13). The scaling parameter  $\gamma_c$  and the order of hyperviscosity  $k$  are given in Table 4.1. The goal when choosing  $k$  is to damp the higher spurious eigenmodes of  $\operatorname{diag}(\omega(\theta)) D_\lambda$  while leaving the lower physical modes that can be resolved by the stencil intact. In this process, the eigenvalues will be pushed into the left half of the complex plane. Then,  $\gamma_c$  is used to condense the eigenvalues as near to the imaginary axis as possible. Figure 4.1b shows the effect of hyperviscosity on the eigenvalues of the DM,  $-\operatorname{diag}(\omega(\theta)) D_\lambda$ , in (4.2).

In order to scale to large node sets, the RBF shape parameter,  $\epsilon$ , is chosen such that the mean condition number of the local RBF interpolation matrices  $\bar{\kappa}_A = \frac{1}{N} \sum_{j=1}^N (\kappa_A)_j$  is kept constant as  $N$  increases (( $(\kappa_A)_j$  is the condition number of the interpolation matrix in ??), representing the  $j^{th}$  stencil). For a constant mean condition number,  $\epsilon$  varies linearly with  $\sqrt{N}$  (see [27] Figure 4a and b). This is not surprising since the condition number strongly depends on the quantity  $\epsilon r$ , where  $r \sim 1/\sqrt{N}$  on the sphere. Thus, to obtain a constant condition number, we let  $\epsilon(N) = c_1 \sqrt{N} - c_2$ , where  $c_1$  and  $c_2$  are constants based on [27].

Table 4.1: Values for hyperviscosity and the RBF shape parameter  $\epsilon$  for vortex roll-up test.

Stencil Size ( $n$ )	$\epsilon = c_1\sqrt{N} - c_2$		$H = -\gamma_c N^{-k} \Delta^k$	
	$c_1$	$c_2$	$k$	$\gamma_c$
17	0.026	0.08	2	8
31	0.035	0.1	4	800
50	0.044	0.14	4	145
101	0.058	0.16	4	40

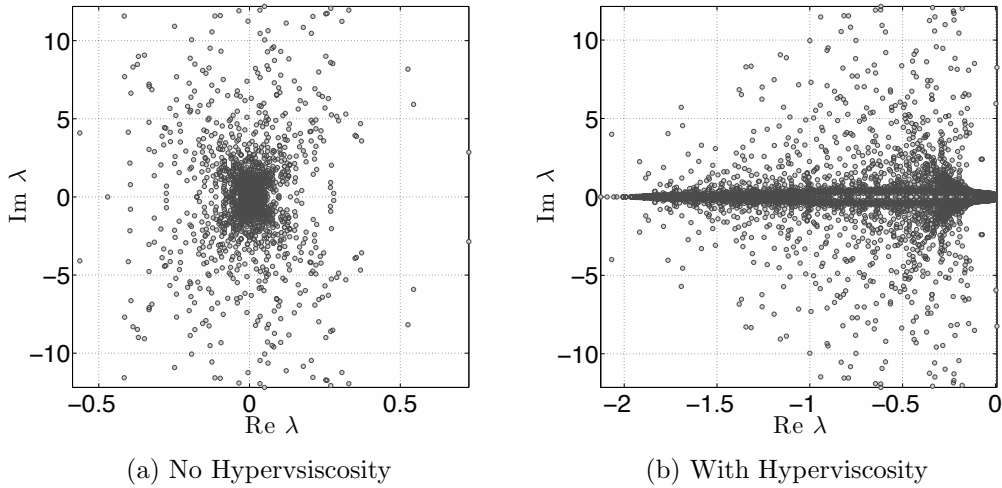


Figure 4.1: Eigenvalues of  $\text{diag}(\omega(\theta))D_\lambda$  for the vortex roll-up test case for  $N = 4096$  nodes, stencil size  $n = 101$  and  $\epsilon = 3.5$ . Left: no hyperviscosity. Right: hyperviscosity enabled with  $k = 4$  and  $\gamma_c = 40$ .

Figure 4.2 shows the solution to Equation (4.1) at  $t = 10$ , on  $N = 10201$  nodes, with stencil size  $n = 50$ . This resolution is sufficient to properly capture the vortices at  $t = 10$ , but lower resolutions would suffer approximation errors associated with insufficient grid resolution. For this reason, the solution at  $t = 3$  is considered in the normalized  $\ell_2$  error convergence study presented in Figure 4.3. The time step  $\Delta t = 0.05$  for all resolutions.

#### 4.4.2 Solid body rotation

The second test case simulates the advection of a cosine bell over the surface of a unit sphere at an angle  $\alpha$  relative to the pole of a standard latitude-longitude grid. The governing PDE is

$$\frac{\partial h}{\partial t} + \frac{u}{\cos \theta} \frac{\partial h}{\partial \lambda} + v \frac{\partial h}{\partial \theta} = 0, \quad (4.3)$$

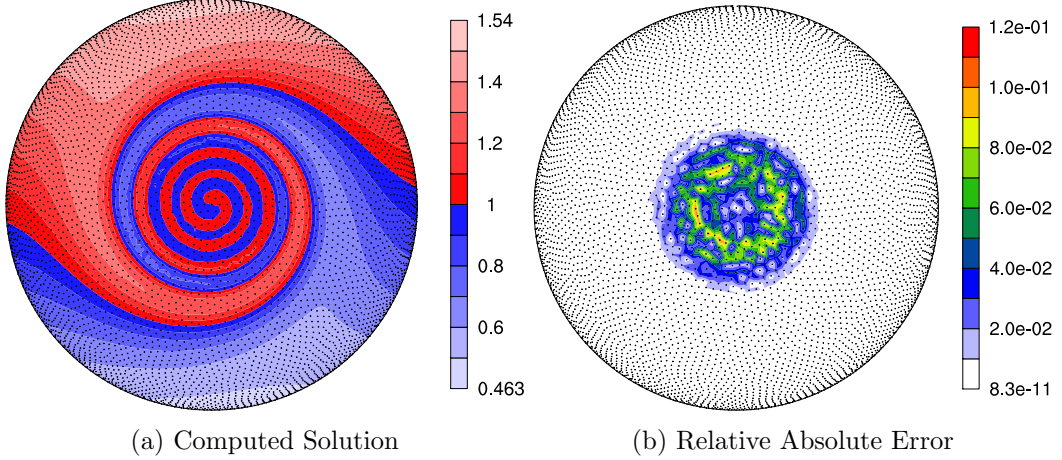


Figure 4.2: Vortex roll-up solution at time  $t = 10$  using RBF-FD with  $N = 10, 201$  and  $n = 50$  point stencil. Normalized  $\ell_2$  error of solution at  $t = 10$  is  $1.25(10^{-2})$

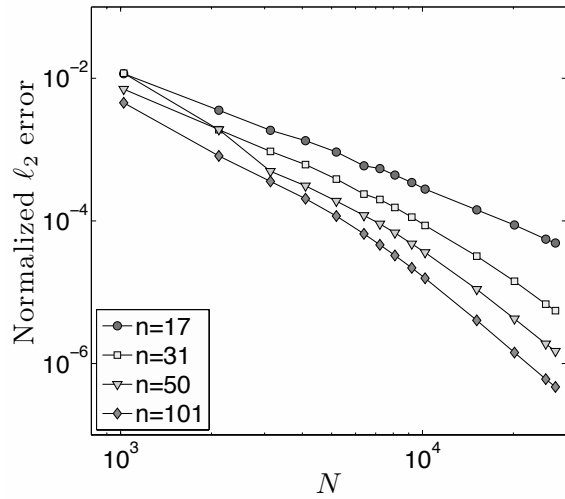


Figure 4.3: Convergence plot for vortex roll-up at  $t = 3$ .

with velocity field,

$$\begin{cases} u = u_0(\cos \theta \cos \alpha + \sin \theta \cos \lambda \sin \alpha), \\ v = -u_0(\sin \lambda \sin \alpha) \end{cases} .$$

inclined at an angle  $\alpha$  relative to the polar axis and velocity  $u_0 = 2\pi/(1036800 \text{ seconds})$  to require 12 days per revolution of the bell as in [54, 28].

The discretized form of (4.3) is

$$\frac{d\mathbf{h}}{dt} = -\text{diag}\left(\frac{u}{\cos \theta}\right) D_\lambda \mathbf{h} - \text{diag}(v) D_\theta \mathbf{h} \quad (4.4)$$

where DMs  $D_\lambda$  and  $D_\theta$  contain RBF-FD weights corresponding to all  $N$  stencils that approximate  $\frac{\partial}{\partial \lambda}$  and  $\frac{\partial}{\partial \theta}$  respectively. Rather than merge the differentiation matrices in (4.4) into one operator, our implementation evaluates them as two sparse matrix-vector multiplies. The separate matrix-vector multiplies are motivated by an effort to provide general and reusable GPU kernels. Additionally, they artificially increase the amount of computation compared to the vortex roll-up test case to simulate cases when operators cannot be merged into one DM (e.g., a non-linear PDE).

By splitting the DM, the singularities at the poles ( $1/\cos \theta \rightarrow \infty$  as  $\theta \rightarrow \pm \frac{\pi}{2}$ ) in (4.3) remain. However, in this case, the approach functions without amplification of errors because the MD node sets have nodes near, but not on, the poles. As noted in [28, 34], applying the entire spatial operator to the right hand side of Equation ?? generates a single DM that analytically removes the singularities at poles.

We will advect a  $C^1$  cosine bell height-field given by

$$h = \begin{cases} \frac{h_0}{2}(1 + \cos(\frac{\pi\rho}{R})) & \rho \leq R \\ 0 & \rho \geq R \end{cases}$$

having a maximum height of  $h_0 = 1$ , a radius  $R = \frac{1}{3}$  and centered at  $(\lambda_c, \theta_c) = (\frac{3\pi}{2}, 0)$ , with  $\rho = \arccos(\sin \theta_c \sin \theta + \cos \theta_c \cos \theta \cos(\lambda - \lambda_c))$ . The angle of rotation,  $\alpha = \frac{\pi}{2}$ , is chosen to transport the bell over the poles of the coordinate system.

Table 4.2: Values for hyperviscosity and RBF shape parameter for the cosine bell test.

Stencil Size ( $n$ )	$\epsilon = c_1 \sqrt{N} - c_2$		$H = -\gamma_c N^{-k} \Delta^k$	
	$c_1$	$c_2$	$k$	$\gamma_c$
17	0.026	0.08	2	$8 * 10^{-4}$
31	0.035	0.1	4	$5 * 10^{-2}$
50	0.044	0.14	6	$5 * 10^{-1}$
101	0.058	0.16	8	$5 * 10^{-2}$

Figure 4.4 compares eigenvalues of the DM for  $N = 4096$  nodes and stencil size  $n = 101$  before and after hyperviscosity is applied. To avoid scaling effects of velocity on the eigenvalues, they have been scaled by  $1/u_0$ . The same approach as in the vortex roll-up case is used to determine the parameters for hyperviscosity and  $\epsilon$ . Our tuned parameters are presented in Table 4.2.

Figure 4.5 shows the cosine bell transported ten full revolutions around the sphere. Without hyperviscosity, RBF-FD cannot complete a single revolution of the bell before instability takes over. However, adding hyperviscosity allows computation to extend to dozens or even thousands of revolutions and maintain stability (e.g., see [34]). After ten revolutions, the cosine bell is still intact. The majority of the absolute error (Figure 4.5b)

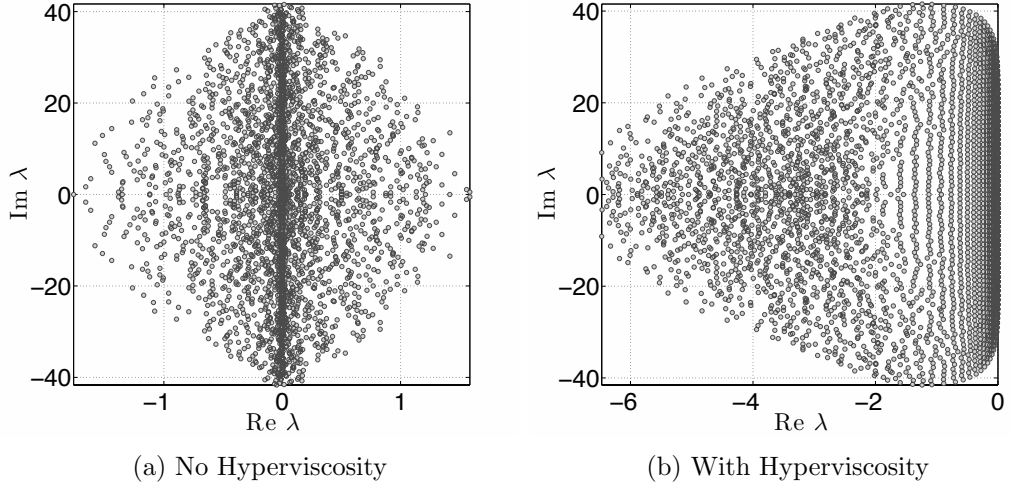


Figure 4.4: Eigenvalues of (4.4) for the cosine bell test case with  $N = 4096$  nodes, stencil size  $n = 101$ , and  $\epsilon = 3.5$ . Left: no hyperviscosity. Right: hyperviscosity enabled with  $k = 8$  and  $\gamma_c = 5 * 10^{-2}$ . Eigenvalues are divided by  $u_0$  to remove scaling effects of velocity.

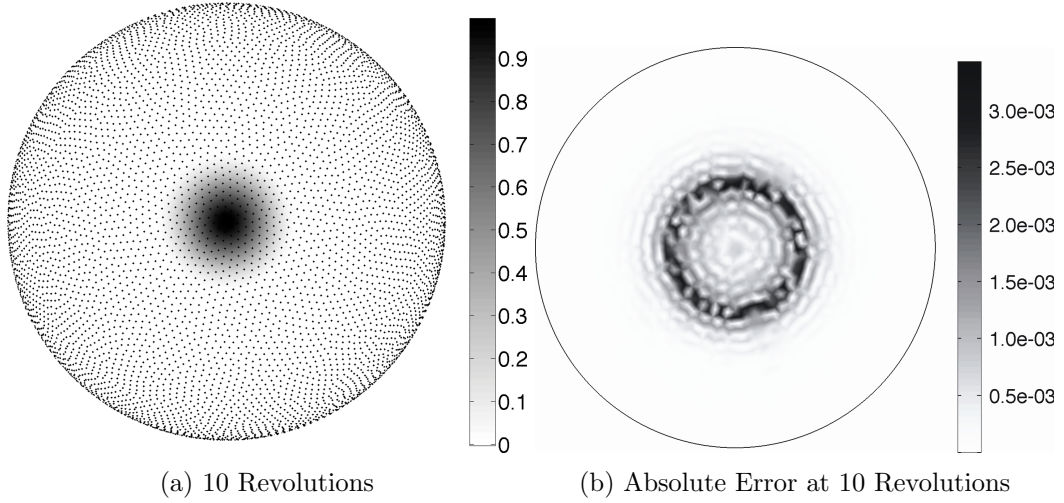


Figure 4.5: Cosine bell solution after 10 revolutions with  $N = 10201$  nodes and stencil size  $n = 101$ . Hyperviscosity parameters are  $k = 8$ ,  $\gamma_c = 5(10^{-2})$ .

appears at the base of the  $C^1$  bell where the discontinuity appears in the derivative. At ten revolutions, Figure 4.6 illustrates the convergence of the RBF-FD method. All tests in Figure 4.6 assume 1000 time-steps per revolution (i.e.,  $\Delta t = 1036.8$  seconds).

**Complete:** 17.28 minutes was a conservative step that allowed the problem to scale

up to  $N = 27556$  nodes. Compare this to the conservative 30 minute time-step taken for  $N = 4096$  nodes in [28], which was already half necessary for DG and 8x less than necessary for both Spherical Harmonics and Double Fourier methods. **Author's Note:** It would be good to quantify the appropriate  $dt$  that would compare RBF-FD to their  $N = 4096$  case with global RBFs.

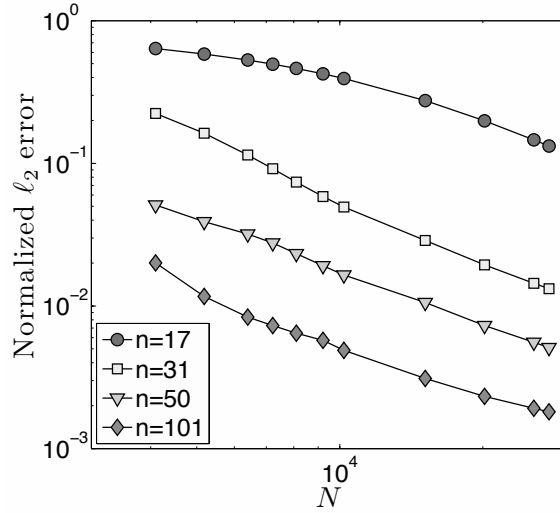


Figure 4.6: Convergence plot for cosine bell advection. Normalized  $\ell_2$  error at 10 revolutions with hyperviscosity enabled.

## 4.5 Fragments (integrate above)

To verify our multi-CPU and multi-CPU+GPU implementations, two hyperbolic PDEs on the surface of the sphere are tested. For both cases a spherical coordinate system is used in terms of latitude  $\lambda$  and longitude  $\theta$ :

$$\begin{aligned} x &= \rho \cos \lambda \cos \theta, \\ y &= \rho \sin \lambda \cos \theta, \\ z &= \rho \sin \theta. \end{aligned}$$

Node sets are the Maximum Determinant point distributions on the sphere [66] consistent with previously published results (see e.g., [?] and [?]).

Hyperviscosity parameters  $\gamma_c$  and  $k$  depend on the RHS of the PDE. For this test case, hyperviscosity scaling parameters are listed in Table 4.1. Linear functions to choose the RBF support parameter  $\epsilon$  are also provided. The parameters  $\gamma_c$  and  $k$  were obtained via trial-and-error parameter searching on  $N = 4096$  nodes. The goal when choosing parameters is to push all eigenvalues to the left half-plane, and then tweak  $\gamma_c$  up or down to condense the eigenvalues as near to the imaginary axis as possible. We try to keep the range of filtered

eigenvalue real parts within twice the width of the unfiltered range, so hyperviscosity does not cause too much diffusion in the solution.

For the cosine bell we use the initial conditions

$$h = \begin{cases} \frac{h_0}{2}(1 + \cos(\frac{\pi\rho}{R})) & \rho \leq R \\ 0 & \rho \geq R \end{cases}$$

where the bell of radius  $R = \frac{a}{3}$  is centered at  $(\lambda_c, \theta_c)$  and provided by the expression,

$$\rho = a \arccos(\sin \theta_c \sin \theta + \cos \theta_c \cos \theta \cos(\lambda - \lambda_c)).$$

We assume  $a = 1$ ,  $h_0 = 1$ , and  $(\lambda_c, \theta_c) = (3\pi/2, 0)$ . The angle  $\alpha = \pi/2$  is chosen to transport the bell over the poles of the coordinate system, and  $u_0 = 2\pi a / 1036800$ .

Author's Note: Include figures from NCL or Paraview

## 4.6 Elliptic

# CHAPTER 5

## PERFORMANCE BENCHMARKS

**Author's Note:** First I need to describe the hardware used. This includes: Troi, Spear, Keeneland; their gpus and RAM, etc. Discuss interconnects (why can't we run multiple kernels on one node of spear)

We present our implementation of an efficient multi-node, multi-GPU RBF PDE package to run on clusters of GPU compute nodes. Each compute node has one or more GPUs attached. Specifically, we utilize the hardware available in the FSU HPC Spear cluster and the NFS funded Keeneland project. While the Spear cluster is only a handful of nodes with 2 GPUs each, Keeneland boasts a total of 240 CPUs and 320 GPUs. The large scale of Keeneland allows us to verify the scaling of our method.

### 5.1 OpenCL

We leverage the OpenCL language for functional portability.

Our dedication to OpenCL is a hedged bet that the future architectures will merge in the middle between many and multi-core architectures with co-processors alongside CPUs. By selecting an open standard parallel programming language, we increase the likelihood for future support of our programs.

#### 5.1.1 OpenCL vs CUDA

The market is volatile. Companies survive by investing margins in their next great product. If a product fails or the company faces a recall, their survival may come into question. Thus far, NVidia's CUDA has been wildly popular, but for the longest time (until May 2012) it was closed source. The closed source limited the language to NVidia hardware. As such, the OpenCL language gained popularity due to its support for AMD, Intel, mobile devices, web browsers, etc. NVidia's push to provide an open source compiler may be an attempt to regain the market share, but OpenCL appears to be on good footing. One other point: with an open source NVidia compiler, OpenCL can be optimized by the more mature NVidia compiler for their proprietary hardware. OpenCL compilers are also becoming more sophisticated at auto-optimization.

	Fermi	GT200
# of concurrent kernels	16	1
Warps scheduled concurrently	2	1
Clock cycles to dispatch instruction to warp	2	4
Caching on Global Device Memory	Yes	No
Shared memory	64 KB	16 KB
Shared memory banks	32	16
Bank conflict free FP64 access	Yes	No
Cycles to read FP64 (from shared memory)	2	32
Max allowed warps	48	32

Table 5.1: Comparison of NVidia's new Fermi architecture to the GT200 architecture used for GTX 280, Tesla C1060 and other GPUs in use today.

### 5.1.2 Asynchronous Queueing

Provide details and simple example of how asynchronous queueing can be used.

Need a figure showing the overlapping comm and comp in a general process with the wait points marked.

## 5.2 Fermi Architecture

In Spring 2010, NVidia will publicly release a new architecture code named "Fermi" [?]. The new hardware will support many features of interest, the most important being 8x faster double precision than the older Tesla C1060 (GT200 architecture). It will also allow for concurrent kernel execution (for up to 16 small kernels) making it easier to keep the GPU saturated with computation. Table 5.1 considers some of the more monumental differences between the Fermi and GT200 architectures.

### 5.2.1 Double Precision

Double precision operations take XXX cycles

### 5.2.2 Local Caching

Local caching allows us to bypass the need for

### 5.2.3 Multiple Kernel Scheduling

describe fermi's ability to schedule multiple kernels, what it means for our queues. Do we need multiple queues, or just one that is non-blocking. How do we indicate we are done communicating if there is no queue to add markers to?

### 5.2.4 Future NVidia Hardware

The latest hardware is the Kepler. It supports the following features

## 5.3 HPC Spear Cluster

## 5.4 Keeneland

## 5.5 Future Hardware

These figures represent optimizations of the Cosine Bell and Vortex Roll-up test cases. Essentially, the optimizations here are general for multi-GPU SpMV. Improving these test cases improves all explicit schemes for RBF-FD (i.e., hyperbolic and parabolic equations, and various time stepping schemes like euler, RK4, Adams-Bashforth etc.).

For the MPI I might need to have multiple figures comparing performance. However, for the GPU optimizations I can show a single plot with all the curves on it. These sections will be good

## 5.6 MPI\_Alltoallv

Change send/recv to alltoallv. Track wait time. Show limitation on scalability with GPU (sublinear) vs CPU (linear). How high can we get linear on CPU?

Communication between processors requires each processor to iterate through their neighboring processors and share information. This can be seen as a simple for loop allowing every processor to touch its neighbors in round-robin fashion. The benchmarks seen in [Author's Note: figures from paper1](#) show the strong scaling of our implementation with a for loop and send/recv.

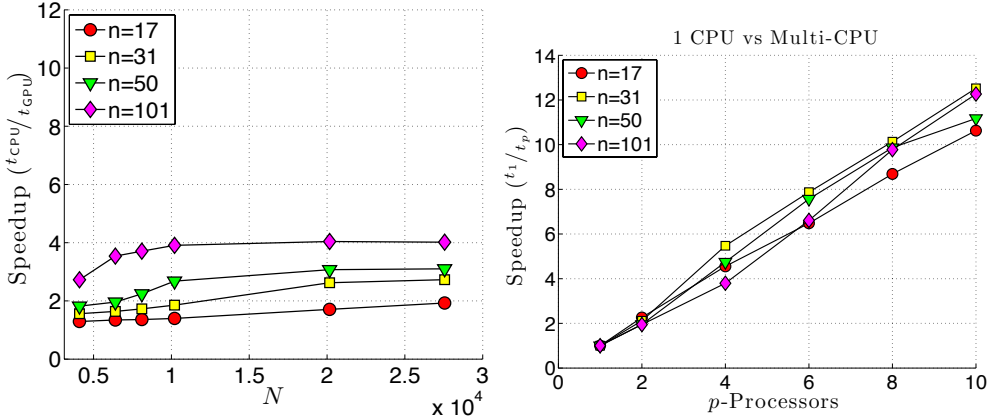
In Figs ?? we show the strong scaling of the cosine bell after

Alternatively

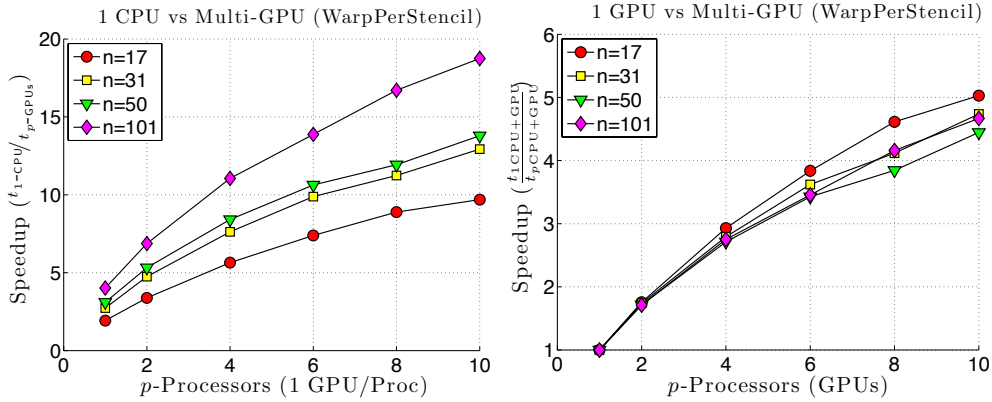
an all to all collective. That is, all processors share some information with potentially every other processor.

[Author's Note: cleanup:](#) These results were run on Keeneland. The changes to MPI communication are the result of changing from blocking communication (MPI\_send/MPI\_recv) to non-blocking communication (MPI\_alltoall).

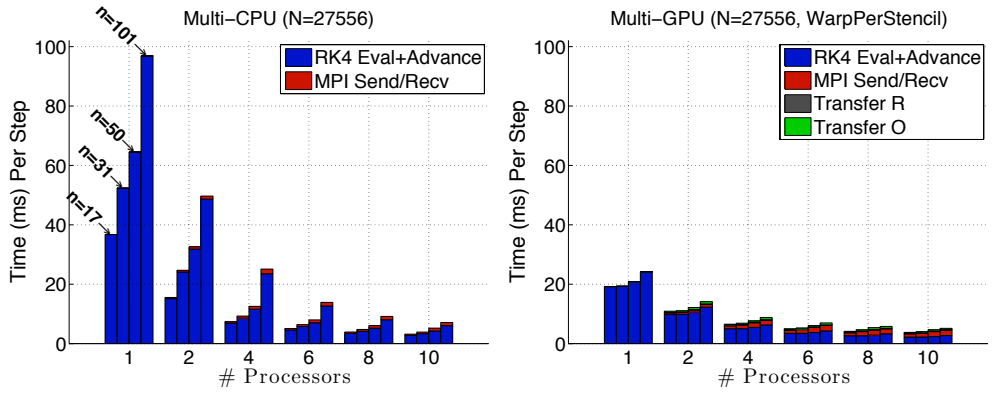
Figure 5.1a shows that our GPU kernel is not much different than in the paper. I have a list of optimizations I'm going through, but this test case focuses on improving the communication.



(a) One warp per stencil kernel on one GPU in Keeneland (b) Multi-CPU strong scaling on Keeneland for one warp per stencil



(c) Multi-GPU strong scaling vs one CPU on Keeneland for one warp per stencil (d) Multi-GPU strong scaling vs one GPU on Keeneland for one warp per stencil



(e) Multi-CPU benchmarks by component on Keeneland (f) Multi-GPU benchmarks by component on Keeneland

Figure 5.1b shows the strong scalability of our method on Multiple CPUs. In distributed computing, ideal scaling is linear. This figure demonstrates that our method does scale linearly (almost super-linearly) as the number of CPUs increases, so our prospect for spanning all CPUs on Keeneland is within reach for problem sizes large enough. The super-linear speedup seen for 10 processors results from improved caching on processors as their individual problem sizes decrease and the processors are able to keep a larger percentage of the problem within fast cache memory.

Figure 5.1c shows the scaling of multiple GPUs vs 1 CPU. Ideally, this figure would be the product of the previous two figures since the GPUs are attached to CPUs in a one to one correspondence. However, we see from the sub-linear scaling that while the GPU accelerators are decreasing the time to compute solutions, there is less and less return of investment as the number of processors increase. Between this Figure and the previous, the only thing that differs is the hardware on which stencils are evaluated. The cost of communication stays the same as in the previous figure. But that means the communication consumes a increasing percentage of the iteration time, until it dominates. Additionally, computing on the GPU requires transfer (additional communication) of data between CPU and GPU.

Figure 5.1d shows the scalability of multiple GPUs vs 1 GPU. Here we see a sub-linear behavior for all cases. This is attributed to both the cost of transfer between CPUs and GPUs and the decreasing problem size as number of processors increases, which underutilizes the GPUs.

Figure 5.1e and Figure 5.1f show the smaller percentage of time per iteration dedicated to communication compared to the figures in the paper. In the Figure 5.1f, the way the times bottom out indicates we are/have converged on the minimum time required to launch a GPU kernel, transfer to/from the GPU, and communicate the problem via MPI. To scale to more processors, a larger problem size is absolutely necessary.

I am generating another set of figures that demonstrate the scaling when we overlap communication and computation. MPI collectives do not allow overlap, but the asynchronous GPU kernel launches do. Therefore, I expect:

- the scaling on multiple CPUs vs 1 CPU to be the same as it is now
- the scaling on multiple GPUs vs 1 GPU will improve to linear/super-linear for problem sizes that occupy the hardware longer than the minimum kernel launch time. For N=27556 we might only see linear speedup up to 6 or 8 processors.
- larger problem sizes will still be necessary (I have benchmarks for 100K, 500K and 1M on the sphere).

## 5.7 Asynchronous OpenCL

What are the limitations if using just async and not the queues?

## 5.8 Multi-Queue OpenCL

How does performance improve if we use two queues (one for Q and one for R)?

## 5.9 GPU Kernel Optimizations

### 5.9.1 Work-Group Size and Number of Stencils

What if a work-group is larger than a warp? What if the group was occupied by multiple stencils. What improvements to speedup do we see?

How many stencils can each group handle (assuming values stay in shared memory)? Shared memory bank conflicts? How do we sort the values? What is the occupancy of the GPU?

### 5.9.2 Parallel Reduction in Shared Memory

What significant gain do we see from adding a segmented scan to the shared memory?  
What other improvements can we think of?

### 5.9.3 Comparison: custom SpMV for explicit schemes vs ViennaCL

# CHAPTER 6

## STOKES

### 6.1 Introduction

We consider herein the solution to steady-state viscous Stokes flow on the surface of a sphere, governed by:

$$\nabla \cdot [\eta(\nabla \mathbf{u} + (\nabla \mathbf{u})^T)] + RaT\hat{r} = \nabla p \quad (6.1)$$

$$\nabla \cdot \mathbf{u} = 0 \quad (6.2)$$

where the unknowns  $\mathbf{u}$  and  $p$  represent the vector velocity- and scalar pressure-field respectively,  $\eta$  is the viscosity tensor,  $Ra$  is the non-dimensional Rayleigh number, and  $T$  is an initial temperature profile. Many practical applications in sciences such as geophysics, climate modeling, and computational fluid dynamics must solve variations of the Navier-Stokes equations. The focus of this paper is on the implicit solve component for viscous (Stokes) flow, which amounts to the steady-state problem described by Equations 6.1 and 6.2.

This article introduces the first (to our knowledge) parallel approach to solve the steady-state equations on the surface of the unit sphere with the Radial Basis Function-generated Finite Differences (RBF-FD) method. Building on our work in [11], which parallelized explicit RBF-FD advection, our goal is to integrate both explicit and implicit components within a larger transient flow model.

**Author's Note:** [follow with details of RBF methods and novelty of RBF-FD.](#)

For decades, the demand for fast and accurate numerical solutions in fluid flow has lead to a plethora of computational methods for various geometries, discretizations and dimensions. On the sphere in  $\mathbb{R}^3$  popular discretizations include the standard latitude-longitude grid, cubed-sphere [54], yin-yang overlapping grid [44], icosahedral grid [58] and centroidal voronoi tessellations [23]. Associate with each discretization is a mesh—specific to the choice of numerical method—that indicates connectivity of nodes for differentiation.

Two decades ago [45], meshless methods based on Radial Basis Functions (RBFs) were introduced for problems that require geometric flexibility with scattered node layouts in  $d$ -dimensional space, plus natural extensions to higher dimensions with minimal change in programming complexity [28, 74]. These RBF methods tout competitive accuracy with other state-of-the-art and high-order methods [28, 29, 26, 74, 25], as well as stability for large time steps. A survey of RBF methods is provided by [25].

**Author's Note:** [Change first sentence](#) RBF-generated finite differences (RBF-FD) hold a promising future in that they share many advantages of global RBF methods, but reduce computational complexity to  $O(N)$  and exhibit increased parallelism. The method was first suggested in 2000 [69], but made its grand debut a few years later in the simultaneous, yet independent, efforts of [65, 68, 73, 14]. It has been successfully employed for a variety of problems including Hamilton-Jacobi equations [14], convection-diffusion problems [15, 67], incompressible Navier-Stokes equations [65, 16], transport on the sphere [34], and the shallow water equations [27].

Compared to classical finite differences (FD) which calculate differentiation weights with one-dimensional polynomials, RBF-FD leverages  $d$ -dimensional RBFs as test functions. This allows for generalization to  $d$ -dimensional space on completely scattered node layouts. For both methods, a stencil of size  $n$  neighboring nodes determines the accuracy of the approximation. However, contrary to the regular stencil node distributions from FD, RBF-FD allows for completely scattered node distributions. In comparison with global RBF methods, spectral accuracy is sacrificed in exchange for computational speed and parallelism. Still, high-order accuracy is possible with RBF-FD—6th- to 10th-order accuracy is common.

Until now, most of the focus in RBF-FD has been on explicit methods. However, many practical applications in sciences such as geophysics, climate modeling, and computational fluid dynamics must solve variations of the navier stokes equations which include an implicit solve component. This paper develops multi-GPU algorithms for implicit RBF-FD systems toward the goal of integration within transient flow problems. The explicit component of transient flow is a natural extension of our work in [9].

**Author's Note:** [Flesh these points out and integrate them in surrounding paragraphs \(until "end"\)](#) Speed not the issue. Need less RBFs for given accuracy of steady state less nodes implies less memory general geometries are supported better distributions of nodes on spheres. competition like CitComS, etc. use cubed sphere, yinyang grids and triangular meshes in combination with low order methods (2nd and 3rd order). Increasing the order of the method or dimension can significantly increase the complexity of the algorithms. RBF-FD naturally extends to higher dimensions and increasing the order is as simple as increasing the number of nodes in the stencil. **Author's Note:** [end](#)

Related work (list references): RBF methods for Elliptic PDEs

- Global [64]
- Compact Support
- divergence-free spherical radial basis Glerkin method for Stokes on the unit sphere [?]
- RBF-FD
  - Incompressible Navier-Stokes using explicit (Euler) and semi-implicit (Crank Nicholson) time step. Small problem size ( $61 \times 61$ ) and small stencil sizes ( $n = 9$ ); ghost nodes beyond boundary strategy. Both RBF-FD and RBF-HFD tested. [16]

Related work on Preconditioned iterative methods for Stokes Flow

- Survey of preconditioners used for Stokes flow problems [52] (limited applicability since they do not assume non-SPD matrices)
- Multi-GPU Jacobi iteration for Navier stokes flow in cavity [http://scholarworks.boisestate.edu/cgi/viewcontent.cgi?article=1003&context=mecheng\\_facpubs](http://scholarworks.boisestate.edu/cgi/viewcontent.cgi?article=1003&context=mecheng_facpubs)

For decades, a major push has been executed in science to parallelize algorithms and leverage resources available on the increasingly capable supercomputers and clusters. Perhaps as soon as the next decade, we will see exascale level architectures ([?]). Given today's technology, those architecture will surely achieve their performance with the help of accelerator hardware such as GPUs.

To prepare the RBF community for the future, we develop algorithms employing two levels of parallelization: first the MPI standard spans computation across multiple CPUs, and second computation is distributed across the many processing cores of GPU accelerators.

The two level parallelization can even be extended to three level parallelism with pThreads or OpenMP [?]. While OpenCL provides the means to target parallelism on either multi-core CPUs or many-core GPUs, it does not allow a parallel kernel on one hardware interact with a parallel kernel on the another. That is to say, an OpenCL kernel on the CPU cannot launch kernels on the GPU s

Our goal is to demonstrate to the geosciences that RBF-FD can function well on both hyperbolic and elliptic problems. In [11] we introduced a multi-GPU implementation of RBF-FD and demonstrated the method's strong ability to stably advect solid bodies on the sphere. In this paper we continue toward the goal of RBF-FD solutions for fluid flow problems with a multi-GPU Poisson solver for steady-state Stokes flow. In this context, speed is not a paramount issue.

Related work on RBF methods targeting the GPU is quite limited. Schmidt et al. [64] solve an implicit system for a global RBF method using Accelerys Jacket in Matlab. Our work in [9] introduced the first parallel implementation of RBF-FD for explicit advection capable of spanning multiple CPUs as well as multiple GPUs.

Related work on multi-CPU or multi-GPU RBFs

- CPU [76] [?]
- single-GPU [64]
- multi-GPU
  - Preconditioned BiCGStab for Navier Stokes, Finite Element method [38]

While RBF-FD differentiation matrices are applied in the same fashion as standard FD methods, they are unique in that they are asymmetric, non-positive definite and potentially have high condition numbers. To solve an implicit system therefore, we requie an iterative krylov solver like GMRES or BiCGStab which are applicable to matrices of this type. Additionally, preconditioned variants of these methods are required to reduce the complexity of the solution process.

Within this paper we implement a preconditioned GMRES method for RBF-FD on multiple GPUs.

Parallel GMRES

- CPU only: PETSc [76], Hypre [?]
- Parallel GMRES on single GPU available in ViennaCL [59] and CUSP [?]
- Parallel GMRES on Multiple GPUs [3]
- Reduced Communication with increased computation [20]

This article continues our effort with an implementation of RBF-FD on both single and multiple-GPUs for elliptic PDEs. In the next section we introduce

## 6.2 RBF-FD Weights

Given a set of function values,  $\{u(\mathbf{x}_j)\}_{j=1}^N$ , on a discrete set of nodes  $\{\mathbf{x}_j\}_{j=1}^N$ , the operator  $\mathcal{L}$  acting on  $u(\mathbf{x}_j)$  is approximated by a weighted combination of function values,  $\{u(\mathbf{x}_i)\}_{i=1}^n$ , in a small neighborhood of  $u(\mathbf{x}_j)$ , where  $n$  defines the size of the stencil and  $n \ll N$ :

$$\mathcal{L}u(\mathbf{x})|_{\mathbf{x}=\mathbf{x}_j} \approx \sum_{i=1}^n w_i u(\mathbf{x}_i) \quad (6.3)$$

The RBF-FD weights,  $w_i$ , are found by enforcing that they are exact within the space spanned by the RBFs  $\phi_i(\epsilon r) = \phi(\epsilon \|\mathbf{x} - \mathbf{x}_i\|)$ , centered at the nodes  $\{\mathbf{x}_i\}_{i=1}^n$ , with  $r = \|\mathbf{x} - \mathbf{x}_i\|$  being the distance between the RBF center and the evaluation point measured in the standard Euclidean 2-norm. It has also been shown through experience and studies [75, 30, 34, 27] that better accuracy is gained by the interpolant being able to reproduce a constant. Hence, the constraint  $\sum_{i=1}^n c_k = \mathcal{L}1|_{\mathbf{x}=\mathbf{x}_j} = 0$  is added, where  $w_{n+1}$  is ignored after the matrix in (6.4) is inverted. That is,

$$\begin{pmatrix} \phi(\epsilon \|\mathbf{x}_1 - \mathbf{x}_1\|) & \phi(\epsilon \|\mathbf{x}_1 - \mathbf{x}_2\|) & \cdots & \phi(\epsilon \|\mathbf{x}_1 - \mathbf{x}_n\|) & 1 \\ \phi(\epsilon \|\mathbf{x}_2 - \mathbf{x}_1\|) & \phi(\epsilon \|\mathbf{x}_2 - \mathbf{x}_2\|) & \cdots & \phi(\epsilon \|\mathbf{x}_2 - \mathbf{x}_n\|) & 1 \\ \vdots & \ddots & \ddots & \vdots & \vdots \\ \phi(\epsilon \|\mathbf{x}_n - \mathbf{x}_1\|) & \phi(\epsilon \|\mathbf{x}_n - \mathbf{x}_2\|) & \cdots & \phi(\epsilon \|\mathbf{x}_n - \mathbf{x}_n\|) & 1 \\ 1 & 1 & \cdots & 1 & 0 \end{pmatrix} \begin{bmatrix} c_1 \\ c_2 \\ \vdots \\ c_n \\ c_{n+1} \end{bmatrix} = \begin{bmatrix} \mathcal{L}\phi(\epsilon \|\mathbf{x} - \mathbf{x}_1\|)|_{\mathbf{x}=\mathbf{x}_j} \\ \mathcal{L}\phi(\epsilon \|\mathbf{x} - \mathbf{x}_2\|)|_{\mathbf{x}=\mathbf{x}_j} \\ \vdots \\ \mathcal{L}\phi(\epsilon \|\mathbf{x} - \mathbf{x}_n\|)|_{\mathbf{x}=\mathbf{x}_j} \\ 0 \end{bmatrix} \quad (6.4)$$

This small system solve is repeated  $N$  times for each  $\mathbf{x}_j$ ,  $j = 1\dots N$ , to form the DM associated with one derivative quantity. As an example, if  $\mathcal{L}$  is the identity operator then the above procedure will lead to RBF-FD interpolation. If  $\mathcal{L}$  is  $\frac{\partial}{\partial x}$ , it will lead to the DM that approximates the first derivative in  $x$ . While Equation 6.4 is symmetric, the added constraints for coefficient  $c_{n+1}$  detracts from the system's positive definite-ness. In lieu of this, a direct LU factorization solves for the weights. Also, observe that multiple right hand sides can be employed to efficiently obtain weights corresponding to all required derivative quantities (i.e.,  $\frac{\partial}{\partial x}$ ,  $\frac{\partial}{\partial y}$ ,  $\nabla^2$ , etc.) in one system solve per stencil center.

## 6.3 GPU Based Solver

Author's Note: We should only discuss the ViennaCL implementation. Unless I can get my ILU preconditioner implemented for CUSP.

Our implementation leverages existing libraries for sparse matrix-vector operations on the GPU. Two libraries exist for sparse matrix linear algebra on the GPU: CUSP [4] and ViennaCL [59]. By implementing our algorithm in the context of ViennaCL, we directly benefit from improvements to the performance of underlying sparse matrix-vector product, vector dot vector and other linear algebra primitives. Also, ViennaCL provides seamless interoperability with the Boost::UBLAS, EIGEN and MTL libraries via C++ templates. We test the performance of our algorithm on one or more CPUs with the Boost::UBLAS library.

### Table comparing CUSP and ViennaCL features

The GMRES algorithm was introduced in 1986 by Saad and Schultz [60]. The iterative solver support general matrix structures, whereas methods like Conjugate Gradient require symmetric positive definiteness.

#### 6.3.1 GMRES Algorithm

At the core of the GMRES algorithm is an Arnoldi (orthogonalization) process. Author's Note: significance of orthogonalization.

Multiple variants of GMRES exist Author's Note: cite refs that utilize unique orthogonalization steps. The motivation behind alternative Arnoldi processes is to save both memory and operation counts. In some cases stability of the GMRES iterations can also be improved Author's Note: I recall a paper saved on my laptop. Saad [60] introduced a practical implementation of the GMRES method that utilizes Given's rotations to compute an implicit QR factorization. The Given's based algorithm is part of the CUSP library; ViennaCL implements the Householder reflection algorithm.

We have implemented the Given's rotation algorithm within ViennaCL, because it is simpler to implement in parallel and increases parallelism Author's Note: verify statement with reference.

[3] does not describe their use of rotations.)

Note that the application of a preconditioner such as ILU0 introduces an additional call to MPI\_Alltoallv before everywhere  $M^{-1}$  is present in Algorithm 6.2.

#### 6.3.2 Multiple GPUs

**Domain Decomposition.** A restricted additive Schwarz [?] domain decomposition is applied. Traditional additive Schwarz methods construct a restriction matrix  $R$  to constrain processor computation to a subdomain and  $R^T$  project it back onto the global domain. In contrast, restricted additive Schwarz replaces the restriction matrix  $R$  with some restriction operator  $R_P^0$  where  $R_P^0 \subset R$ , but continues to use  $R^T$  to project the solution back onto the global domain. The main idea behind re , restricted additive schwarz assigns all nodes to exactly one subdomain. Regular additive Schwarz would allow nodes to be in one or more subdomains.

---

**Algorithm 6.1** Left-preconditioned GMRES(k) with Given's Rotations

---

```

1:  $\varepsilon$  (tolerance for the residual norm  $r$ ),  $x_0$  (initial guess), and set  $convergence = false$ 
2: MPI_Alltoallv( $x_0$ )
3: while  $convergence == false$  do
4:    $r_0 = M^{-1}(b - Ax_0)$ 
5:   MPI_Alltoallv( $r_0$ )
6:    $\beta = \|r_0\|_2$                                  $\triangleright \text{MPI_Allreduce}(<r_0, r_0>)$ 
7:    $v_1 = r_0/\beta$ 
8:   for  $j = 1$  to  $k$  do
9:      $w_j = M^{-1}Av_j$                           $\triangleright \text{MPI_Alltoallv}(< w_j >)$ 
10:    for  $i = 1$  to  $j$  do
11:       $h_{i,j} = < w_j, v_i >$                    $\triangleright \text{MPI_Allreduce}$ 
12:       $w_j = w_j - h_{i,j}v_i$ 
13:    end for
14:     $h_{j+1,j} = \|w_j\|_2$                        $\triangleright \text{MPI_Allreduce}$ 
15:     $v_{j+1} = w_j/h_{j+1,j}$ 
16:  end for
17:  Set  $V_k = [v_1, \dots, v_k]$  and  $\bar{H}_k = (h_{i,j})$  an upper Hessenberg matrix of order  $(m + 1) \times m$ 
18:  Solve a least-square problem of size  $m$ :  $\min_{y \in \mathbb{R}^m} \|\beta e_1 - \bar{H}_k y\|_2$ 
19:   $x_k = x_0 + V_k y_k$ 
20:  if  $\|M^{-1}(b - Ax_k)\|_2 < \varepsilon$  then
21:     $convergence = true$ 
22:  end if
23: end while

```

---

$$\mathbf{u} = \sum_{p=0}^{numprocs} R'_p (A(R_p^0)^T)^{-1} R_p^0 R_P F \quad (6.5)$$

where  $R_p$  is a restriction matrix (identity on diagonals for stencils operated on by a processor, zero elsewhere). In our case, the partitions are determined by node coordinates, so all non-zeros for a stencil row end up on the same processor (i.e., the decomposition of the matrix does not allow multiple domain blocks per row).

**MPI Communication.** Mention communication using MPI\_AlltoAllv, MPI\_Allreduce. (Show communication points in algorithm—be sure to explicitly show Givens rotations in algorithm. [3] did list rotations. We also use the CPU for Gram Schmidt process.)

## 6.4 Multiple GPUs

Scaling GMRES across multiple GPUs requires a domain decomposition. Domain decompositions can be interpreted as partitioning of nodes or cuts along

**Domain Decomposition.** The domain is decomposed naïvely by cutting the domain into domain bounding box into  $P$  equal sized partitions. Each processor is assigned one partition. Partitions may contain unequal number of nodes. Future work will integrate a domain partitioning library such as ParMETIS [?] or SCOTCH [?] to improve load balancing for processors.

$$\mathbf{u} = \sum_{p=0}^{\text{numprocs}} R_p (A R_p^T)^{-1} F \quad (6.6)$$

where  $R_p$  is a restriction matrix (identity on diagonals for stencils operated on by a processor, zero elsewhere). In our case, the partitions are determined by node coordinates, so all non-zeros for a stencil row end up on the same processor (i.e., the decomposition of the matrix does not allow multiple domain blocks per row).

The restriction matrix  $R_p^0$  contains only zeros and ones. Cai et al. [?] let  $R_p^0$  contain ones on the diagonal to indicate rows of the system for which a processor  $p$  is responsible. Our implementation similarly places  $I$  on the diagonal, but we then apply a general permutation matrix  $P$  to compress  $R_p^0 A$  such that processors assemble an  $N_p \times m$  local matrix (where  $N_p \ll N$  and  $m \ll N$ ). Likewise, processors allocate vectors for the reduced problem size. The solution is  $N_p \times 1$  and RHS is  $m \times 1$ . Recall that the domain decomposition is determined by node partitioning, which does not guarantee rows of the global system corresponding to stencils in a processor's partition will be a contiguous block of the full system.

#### 6.4.1 Solution Ordering

To simplify distribution of solution values, we apply a reordering to the system to interleave components of the solution and group solutions by node. This allows us to directly copy a double4 for each

The DM assembly depends on all dimensions of solution values for a single node to be consecutive in memory. While Equation 6.15 has all components of  $U, V, W$  and  $P$  grouped together, the values of  $u_1, v_1, w_1$  and  $p_1$  correspond to node  $(x_1, y_1, z_1)$ .

Figure 6.1 demonstrates the effect of interleaving our solution. The sparsity pattern of the original DM with solutions grouped by component is shown in Figure 6.1a. Well defined blocks of non-zeros are filled with RBF-FD weights from Equation 6.7. Figure 6.1b presents the sparsity pattern for interleaved solution components. The pattern is similar to a single block of Figure 6.1a, but the sub-matrix  $(10 : 50) \times (10 : 50)$  of each solution ordering, shown in Figures 6.1c and 6.1d, illustrate that non-zeros in Figure 6.1b are small  $4 \times 4$  blocks with the structure of Equation 6.7.

**Node Order.** Author's Note: Should we discuss node ordering and its implications on convergence? if so, I should state:

- Nodes are read from file
- Their order is either: unmodified or modified

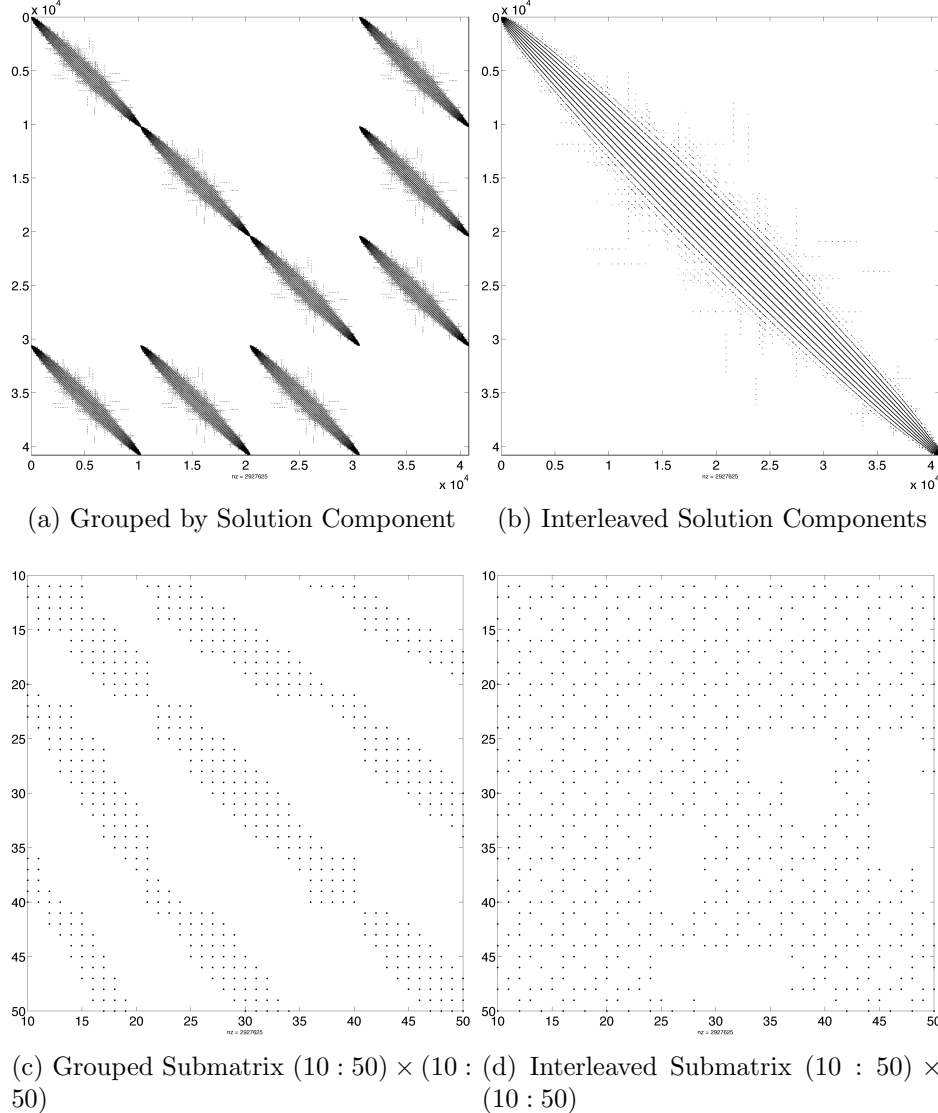


Figure 6.1: Sparsity pattern of linear system in Equation 6.7. Solution values are either ordered by component (e.g.,  $(u_1, \dots, u_N, v_1, \dots, v_N, w_1, \dots, w_N, p_1, \dots, p_N)^T$ ) or interleaved (e.g.,  $(u_1, v_1, w_1, p_1, \dots, u_N, v_N, w_N, p_N)^T$ ).

- If modified, our goal is to improve memory access patterns by reducing the bandwidth of the DM. A bandwidth of  $n$  is the best case scenario where the solution vector is accessed linearly. The worst case scenario is when bandwidth is  $N$  and the solution is accessed randomly via stencils.
- Ordering nodes according to a space filling curve can reduce the “randomness” of solution access by placing elements of stencils nearby (sometimes sequential) in memory.
- Many space filling curves exist. Raster (IJK), Snake, Morton, Hilbert, U, X, etc. We

consider Raster here, with other orderings left for future work.

- Our restriction operator for domain decomposition might reduce the bandwidth for each processor compared to the global DM. How does the combination of restriction and reordering work?
- Reordering the DM has implications on its condition number and the convergence rate of the GMRES algorithm. We should provide bandwidth of matrix before and after reordering, as well as the condition number before and after. We should monitor convergence with and without reordering, and compare the number of GMRES iterations per minute/second.

**MPI Communication.** The majority of communication within our implementation consists of two MPI routines: MPI\_Alltoall and MPI\_Allreduce.

## 6.5 Governing Equations

We solve the PDE on the surface of the sphere as an example for one and multiple GPUs. Boundary conditions detract from the accuracy of RBF-FD and introduce other issues such as Runge phenomena [?], so we first verify the solution without boundaries.

Author's Note: Need to reference work that solves problem in two steps and justify our approach to solve in one step. Golub paper might be good for this. Or the Stoke preconditioners paper

Assuming  $\eta$  is a constant (i.e.,  $\nabla\eta = 0$ ), our system simplifies to

$$\begin{pmatrix} -\eta\nabla^2 & 0 & 0 & \frac{\partial}{\partial x_1} \\ 0 & -\eta\nabla^2 & 0 & \frac{\partial}{\partial x_2} \\ 0 & 0 & -\eta\nabla^2 & \frac{\partial}{\partial x_3} \\ \frac{\partial}{\partial x_1} & \frac{\partial}{\partial x_2} & \frac{\partial}{\partial x_3} & 0 \end{pmatrix} \begin{pmatrix} u_1 \\ u_2 \\ u_3 \\ p \end{pmatrix} = \frac{RaT}{\sqrt{x_1^2 + x_2^2 + x_3^2}} \begin{pmatrix} x_1 \\ x_2 \\ x_3 \\ 0 \end{pmatrix}. \quad (6.7)$$

where the  $\nabla^2$  operator in spherical polar coordinates for  $\mathbb{R}^3$  is:

$$\nabla^2 = \underbrace{\frac{1}{\hat{r}} \frac{\partial}{\partial \hat{r}}}_{\text{radial}} \left( \hat{r}^2 \frac{\partial}{\partial \hat{r}} \right) + \underbrace{\frac{1}{\hat{r}^2} \Delta_S}_{\text{angular}}. \quad (6.8)$$

Here  $\Delta_S$  is the Laplace-Beltrami operator—i.e., the Laplacian constrained to the surface of the sphere with radius  $\hat{r}$ . This form nicely illustrates the components of the  $\nabla^2$  corresponding to the radial and angular terms.

On the surface of the unit sphere the radial term vanishes, so we are left with:

$$\nabla^2 \equiv \Delta_S. \quad (6.9)$$

The following RBF operator from [74]—Equation (20) can be applied to the RHS of Equation 6.4 to generate Laplace-Beltrami RBF-FD weights:

$$\Delta_S = \frac{1}{4} \left[ (4 - r^2) \frac{\partial^2}{\partial r^2} + \frac{4 - 3r^2}{r} \frac{\partial}{\partial r} \right], \quad (6.10)$$

where  $r$  is the Euclidean distance between nodes of an RBF-FD stencil and is independent of our choice of coordinate system.

Additionally following [29, 27], the off-diagonal blocks in Equation 6.7 must be constrained to the sphere via the projection matrix:

$$P = I - \mathbf{x}\mathbf{x}^T = \begin{pmatrix} (1-x_1^2) & -x_1x_2 & -x_1x_3 \\ -x_1x_2 & (1-x_2^2) & -x_2x_3 \\ -x_1x_3 & -x_2x_3 & (1-x_3^2) \end{pmatrix} = \begin{pmatrix} P_{x_1} \\ P_{x_2} \\ P_{x_3} \end{pmatrix} \quad (6.11)$$

where  $\mathbf{x}$  is the unit normal at the stencil center, and [29, 27] show that with a little manipulation weights can be directly computed with these operators for Equation 6.4:

$$P \frac{\partial}{\partial x_1} = (x_1 \mathbf{x}^T \mathbf{x}_k - x_{1,k}) \frac{1}{r} \frac{\partial}{\partial r} |_{\mathbf{x}=\mathbf{x}_j} \quad (6.12)$$

$$P \frac{\partial}{\partial x_2} = (x_2 \mathbf{x}^T \mathbf{x}_k - x_{2,k}) \frac{1}{r} \frac{\partial}{\partial r} |_{\mathbf{x}=\mathbf{x}_j} \quad (6.13)$$

$$P \frac{\partial}{\partial x_3} = (x_3 \mathbf{x}^T \mathbf{x}_k - x_{3,k}) \frac{1}{r} \frac{\partial}{\partial r} |_{\mathbf{x}=\mathbf{x}_j} \quad (6.14)$$

### 6.5.1 Constraints

Due to the lack of boundary conditions on the sphere, the family of solutions that satisfy the PDE in Equation 6.7 includes four free constants (one for each  $u_1, u_2, u_3$  and  $p$ ).

One way to close the null-space of the solution is to augment Equation 6.7 with the following constraints:

$$\left( \begin{array}{cccc|cccc} -\eta \nabla^2 & 0 & 0 & \frac{\partial}{\partial x_1} & 1_{N \times 1} & 0 & 0 & 0 \\ 0 & -\eta \nabla^2 & 0 & \frac{\partial}{\partial x_2} & 0 & 1_{N \times 1} & 0 & 0 \\ 0 & 0 & -\eta \nabla^2 & \frac{\partial}{\partial x_3} & 0 & 0 & 1_{N \times 1} & 0 \\ \frac{\partial}{\partial x_1} & \frac{\partial}{\partial x_2} & \frac{\partial}{\partial x_3} & 0 & 0 & 0 & 0 & 1_{N \times 1} \\ \hline 1_{1 \times N} & 0 & 0 & 0 & | & | & | & | \\ 0 & 1_{1 \times N} & 0 & 0 & | & | & | & | \\ 0 & 0 & 1_{1 \times N} & 0 & | & | & | & | \\ 0 & 0 & 0 & 1_{1 \times N} & | & | & | & | \end{array} \right) \begin{pmatrix} u_1 \\ u_2 \\ u_3 \\ p \\ c_1 \\ c_2 \\ c_3 \\ c_4 \end{pmatrix} = \frac{RaT}{\sqrt{x_1^2 + x_2^2 + x_3^2}} \begin{pmatrix} x_1 \\ x_2 \\ x_3 \\ 0 \\ \int_{\Omega} u_1 \partial \Omega \\ \int_{\Omega} u_2 \partial \Omega \\ \int_{\Omega} u_3 \partial \Omega \\ \int_{\Omega} p \partial \Omega \end{pmatrix}. \quad (6.15)$$

**Author's Note:** Need the integral of my manufactured solution on the RHS.  $\ell_1$  norm does not converge to 0, so it will screw solve with constraints where the subscript on  $1_{N \times 1}$  indicates a  $N \times 1$  vector of ones. These constraints add the unknowns  $(c_1, c_2, c_3, c_4)$ , which should solve to be zero. The four rows on the bottom require that the solution satisfy the integral over the domain for each solution component. In combination with the four added columns, the constraints indicate that the solution components must satisfy integrals using the same constant value. This is only possible if the constants are zero. Our added constraints are not chosen for physical significance, but for algebraic significance. When solving Equation 6.15 with GMRES, the constraints improve conditioning of the system and increase the rate of convergence.

We also investigate the use of GMRES without constraints. This increases the number of iterations required to converge, but allows increased parallelism (decreased data sharing).  
**Author's Note:** Perhaps we can iterate without constraints until convergence slows then "restart" the problem on a single GPU with constraints included? Limits scalability but would allow more parallelism for part of iterations while also reasonable convergence.

### 6.5.2 Manufactured Solution

To verify our implementation, we manufacture a solution that satisfies the continuity equation. Using the identity

$$\nabla \cdot (\nabla \times g(\mathbf{x})) = 0, \quad (6.16)$$

for any function  $g(\mathbf{x})$ , we can easily manufacture a solution by choosing some vector function  $g(\mathbf{x})$ , projecting it onto the sphere via  $P_x g(x)$  and applying the curl projection,  $Q_x$ :

$$Q_x = \begin{bmatrix} 0 & -x_3 & x_2 \\ x_3 & 0 & -x_1 \\ -x_2 & x_1 & 0 \end{bmatrix}. \quad (6.17)$$

Then, a manufactured solution that satisfies both momentum and continuity conditions on the surface of the sphere is given by:

$$\mathbf{u} = Q_x(g(\mathbf{x})) \quad (6.18)$$

Typically, on the surface of the sphere, the projection operator from Equation 6.11 must be applied to an arbitrary  $g(\mathbf{x})$ . Here, we choose the components of  $g(\mathbf{x})$  to be various spherical harmonics in Cartesian coordinates where  $P_x Y_l^m = Y_l^m$ . Consequently, application of  $P_x$  can be ignored.

We select  $g(x)$  to be:

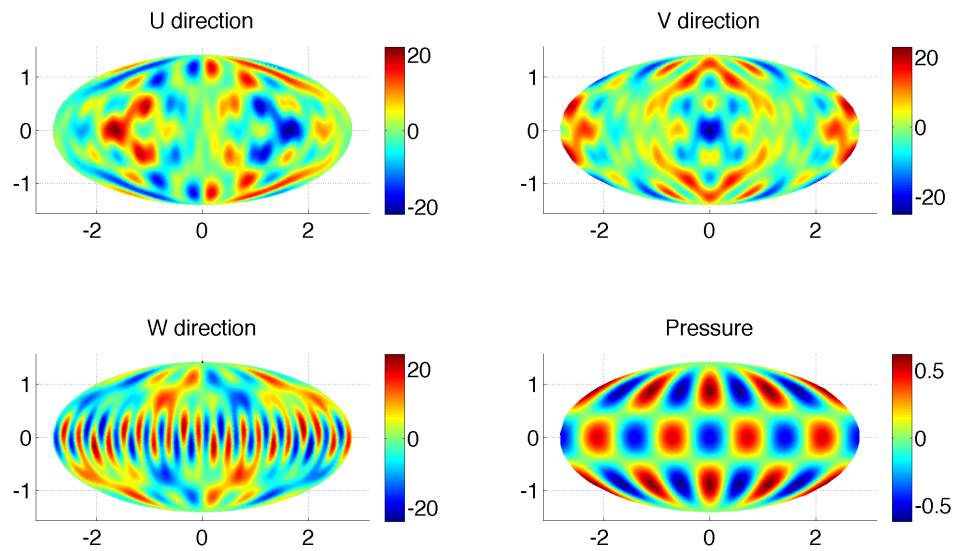
$$g(x) = 8Y_3^2 - 3Y_{10}^5 + Y_{20}^{20} \quad (6.19)$$

and the pressure function:

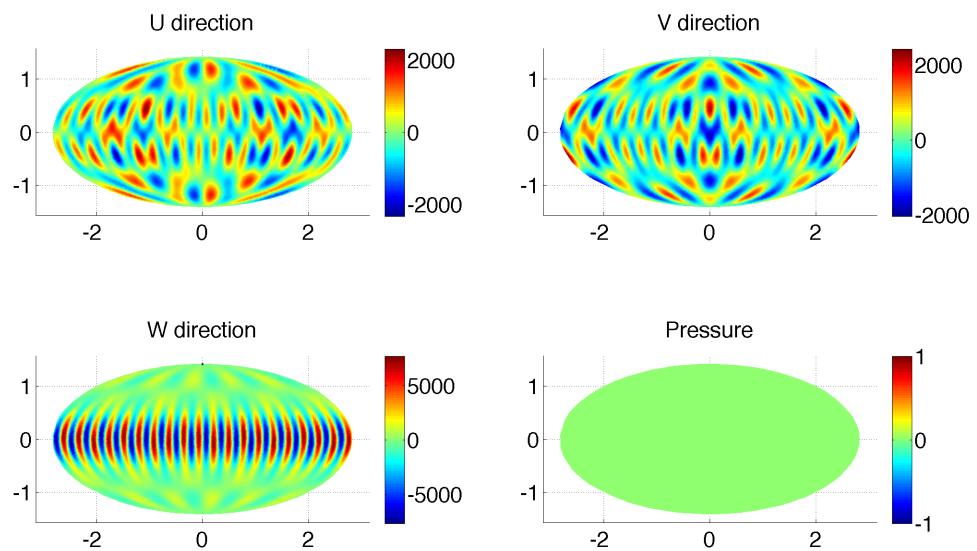
$$P = Y_6^4 \quad (6.20)$$

The manufactured solution is shown in Figure 6.2. A Mollweide projection [?] maps the sphere onto the plane.

**Convergence.** As the problem size  $N$  increases, we expect the approximation to the solution to converge on the order of  $\sqrt{n}$  where  $n$  is the choice of stencil size. Figure ?? demonstrates the convergence of our solution with respect to  $\sqrt{N}$  for stencil sizes  $n = 31, 101$   
**Author's Note:** update when figure is complete.



(a) Solution  $Q_x(g(x))$  with  $g(x) = 8Y_3^2 - 3Y_{10}^5 + Y_{20}^{20}$



(b) Right Hand Side (Constant Viscosity)

Figure 6.2: A divergence free field is manufactured for the sphere.

## 6.6 Preconditioning

GMRES is slow to converge when used without a preconditioner.

The differentiation matrix produced by RBF-FD is asymmetric, non-positive definite, and non-diagonally dominant. Thus, many of the popular choices for preconditioning provided by CUSP and ViennaCL do not apply.

Our tests show that an incomplete LU factorization with zero fill-in [61] functions well.

We also find that a large Krylov subspace must be saved. GMRES converges best when approximately 250 dimensions are saved between restarts.

[Plot comparing residual of GMRES without precond and with ILU0](#)

[Author's Note: Need to comment on the conditioning of the system and how stencils can influence convergence .](#)

Need a table/plot comparing convergence of various preconditioners (ILU0, ILUT, AMG, etc.). We will justify our use of ILU0 even if it is the most basic and frequently least beneficial approach.

Demonstrate ILU0 is best for converging between

- Jacobi
- ILU0 on block ( $1 : 3 * N$ )
- ILU0 on full matrix
- ILUT
- AMG

---

**Algorithm 6.2** Incomplete LU Factorization with Zero Fill-in (ILU0)

---

```
1: for  $i$  do = 0  
2:    $a_{i,i} = a_{i,i}/a_{i,i}$   
3: end for
```

---

## 6.7 GMRES Results

We want to express benchmarks in terms of the number of GMRES iterations per second, and the number of iterations required to converge. Readers wont care what percentage of peak we are getting, just how fast we get to the solution.

- One GPU
  - [Convergence for stokes steady](#)
  - [GMRES iteration plot \(assuming 1e-8 and restart=60\)](#)
- Multi-GPU
  - Number of iterations without constraints
  - Number of iterations with constraints

- GMRES iteration plot
- plot: number of GMRES iterations per second w.r.t. number of processors

## 6.8 Fragments

Need to describe the solver.

State that the conditions under which a problem is solved determines how quickly it will converge. For example, nodes too close together on delaunay meshes cause higher condition numbers and require more iterations. Proper choice of preconditioners can dramatically reduce the number of iterations required to converge. Although preconditioners incur an additional cost in preprocessing and at each iteration of the solver, the potential number of iterations they save

# CHAPTER 7

## COMMUNITY OUTREACH

- Evan F. Bollig, Natasha Flyer, and Gordon Erlebacher. Using Radial Basis Function Finite Difference (RBF-FD) for PDE Solutions on the GPU. *in press. Elsevier J. Comput. Phys.*, 2012
- Evan F. Bollig, Natasha Flyer, and Gordon Erlebacher. Solving Elliptic PDEs with RBF-generated Finite Differences on Multiple GPUs. *in preparation*, 2012
- E. F. Bollig. Multi-GPU Solutions of Hyperbolic and Elliptic PDEs with RBF-FD. Contributed Talk. SIAMSEAS Annual Meeting. Huntsville, AL, March 2012
- E. F. Bollig. Parallel Algorithms for RBF-FD Solutions to PDEs on the Sphere. Poster. FSU Dept. of Sci. Comp. Computational Xpo. Tallahassee, FL, March 2012
- E. F. Bollig. A Multi-CPU/GPU implementation of RBF-generated finite differences for PDEs on a Sphere. Poster. American Geophys. Union. San Francisco, CA, December 2011
- E. F. Bollig. Accelerating RBF-FD in Parallel Environments. Student Presentation. NSF CBMS Workshop: Radial Basis Functions Mathematical Developments and Applications. Darmouth, MA, June 2011

need Survey of goals stated in prospectus and whether they were completed or not (Probably part of slides, not actual dissertation)

## APPENDIX A

### AVOIDING POLE SINGULARITIES WITH RBF-FD

This content follows [28, 29].

Within the test cases of this dissertation, we solve convective PDEs on the unit sphere with the form:

$$\frac{\partial h}{\partial t} = \mathbf{u} \cdot \nabla h$$

where  $\mathbf{u}$  is velocity. For example, the cosine bell advection has this particular form:

$$\frac{\partial h}{\partial t} = \frac{u}{\cos \theta} \frac{\partial h}{\partial \lambda} + v \frac{\partial h}{\partial \theta} \quad (\text{A.1})$$

in the spherical coordinate system defined by

$$\begin{aligned} x &= \cos \theta \cos \lambda \\ y &= \cos \theta \sin \lambda \\ z &= \sin \theta \end{aligned}$$

where  $\theta \in (-\frac{\pi}{2}, \frac{\pi}{2})$  is the elevation angle and  $\lambda \in (-\pi, \pi)$  is the azimuthal angle. Observe that as  $\theta \rightarrow \pm \frac{\pi}{2}$ , the  $\frac{1}{\cos \theta}$  term goes to infinity as a discontinuity.

One of the many selling points for RBF-FD and other RBF methods is their ability analytically avoid pole singularities, which arise from the choice of coordinate system and not from the methods themselves. Since RBFs are inherently based on Euclidean distance between nodes, and not geodesic distance, they do not “feel” the effects of the geometry or recognize singularities naturally inherent in the coordinate system [28]. Here we demonstrate how pole singularities are analytically avoided with RBF-FD for cosine bell advection.

Let  $r = \|\mathbf{x} - \mathbf{x}_j\|$  be the Euclidean distance which is invariant of the coordinate system. In Cartesian coordinates, we have

$$r = \sqrt{(x - x_j)^2 + (y - y_j)^2 + (z - z_j)^2}.$$

In spherical coordinates we have:

$$r = \sqrt{2(1 - \cos \theta \cos \theta_j \cos(\lambda - \lambda_j) - \sin \theta \sin \theta_j)}.$$

The RBF-FD operators for  $\frac{d}{d\lambda}, \frac{d}{d\theta}$  are discretized with the chain rule:

$$\frac{d\phi_j(r)}{d\lambda} = \frac{dr}{d\lambda} \frac{d\phi_j(r)}{dr} = \frac{\cos \theta \cos \theta_j \sin(\lambda - \lambda_j)}{r} \frac{d\phi_j(r)}{dr}, \quad (\text{A.2})$$

$$\frac{d\phi_j(r)}{d\theta} = \frac{dr}{d\theta} \frac{d\phi_j(r)}{dr} = \frac{\sin \theta \cos \theta_j \cos(\lambda - \lambda_j) - \cos \theta \sin \theta_j}{r} \frac{d\phi_j(r)}{dr}, \quad (\text{A.3})$$

where  $\phi_j(r)$  is the RBF centered at  $\mathbf{x}_j$ .

Plugging A.2 and A.3 into A.1, produces the following explicit form:

$$\frac{dh}{dt} = u(\cos \theta_j \sin(\lambda - \lambda_j) \frac{1}{r} \frac{d\phi_j}{dr}) + v(\sin \theta \cos \theta_j \cos(\lambda - \lambda_j) - \cos \theta \sin \theta_j \frac{1}{r} \frac{d\phi}{dr})$$

where  $\cos \theta$  from A.2 analytically cancels with the  $\frac{1}{\cos \theta}$  in A.1.

Then, formally, one would assemble differentiation matrices containing weights for the following operators:

$$\mathbf{D}_\lambda = \cos \theta_j \sin(\lambda - \lambda_j) \frac{1}{r} \frac{d\phi_j}{dr}, \quad (\text{A.4})$$

$$\mathbf{D}_\theta = \sin \theta \cos \theta_j \cos(\lambda - \lambda_j) - \cos \theta \sin \theta_j \frac{1}{r} \frac{d\phi}{dr}, \quad (\text{A.5})$$

and solve the explicit method of lines problem:

$$\frac{dh}{dt} = u\mathbf{D}_\lambda h + v\mathbf{D}_\theta h$$

where now the system is completely free of singularities at the poles [29].

We note that the expression  $\cos(\frac{\pi}{2})$  evaluates on some systems to a very small number rather than zero (e.g.,  $6.1(10^{-17})$  on the Keeneland system and GNU gcc toolchain). The small value in turn allows  $\frac{1}{\cos \theta}$  to evaluate to a large value (e.g.,  $1.6(10^{16})$ ) rather than “inf” or “NaN”. The large value allows the cosine terms to cancel in double precision, whereas an “inf” or “NaN” would corrupt the solution. Rather than avoid placing nodes at the poles, or assuming the machine will numerically cancel the singularities, it is preferred to use operators A.4, A.5 on the RHS of Equation 2.3.

# APPENDIX B

## PROJECTED WEIGHTS ON THE SPHERE

It is shown in [29, 27] that a projection operator

$$\mathbf{P} = \mathbf{I} - \mathbf{x}\mathbf{x}^T = \begin{bmatrix} (1-x^2) & -xy & -xz \\ -xy & (1-y^2) & -yz \\ -xz & -yz & (1-z^2) \end{bmatrix} = \begin{bmatrix} \mathbf{p}_x^T \\ \mathbf{p}_y^T \\ \mathbf{p}_z^T \end{bmatrix}$$

where  $\mathbf{p}_x^T$  represents the projection operator in the  $x$  direction.

From [29], the projected RBF gradient operator is:

$$\begin{aligned} \mathbf{P} \cdot \nabla \phi_k(r(\mathbf{x})) &= \mathbf{P} \cdot \frac{(\mathbf{x} - \mathbf{x}_k)}{r(\mathbf{x})} \frac{d\phi_k(r(\mathbf{x}))}{dr(\mathbf{x})} \\ &= -\mathbf{P} \cdot \mathbf{x}_k \frac{1}{r(\mathbf{x})} \frac{d\phi_k(r(\mathbf{x}))}{dr(\mathbf{x})} \end{aligned} \quad (\text{B.1})$$

$$= \begin{bmatrix} x\mathbf{x}^T \mathbf{x}_k - x_k \\ y\mathbf{x}^T \mathbf{x}_k - y_k \\ z\mathbf{x}^T \mathbf{x}_k - z_k \end{bmatrix} \frac{1}{r(\mathbf{x})} \frac{d\phi(r(\mathbf{x}))}{dr}. \quad (\text{B.2})$$

The operator  $\mathbf{I} - \mathbf{x}\mathbf{x}^T$  for  $\mathbf{x} = (x, y, z)$  projects a vector onto the plane tangent to the unit sphere at  $(x, y, z)$ . Therefore, Equation B.2 gives the projection of the gradient operator at  $\mathbf{x}_k$  onto the plane tangent to  $\mathbf{x}$ .

### B.1 Direct Weights

Following [27], B.2 takes on the following when adapted to RBF-FD:

$$[\mathbf{p}_x \cdot \nabla f(\mathbf{x})]|_{\mathbf{x}=\mathbf{x}_c} = \sum_{k=1}^n c_k \underbrace{\left[ x_c \mathbf{x}_c^T \mathbf{x}_k - x_k \right]}_{B_{c,k}^{\mathbf{p}_x}} \frac{1}{r} \frac{d\phi(r(x_c))}{dr}. \quad (\text{B.3})$$

and so forth for the  $\mathbf{p}_y, \mathbf{p}_z$  operators, where  $\mathbf{x}_c$  is the stencil center and  $\mathbf{x}_k$  are stencil nodes. To compute RBF-FD weights for the  $\mathbf{p}_x$  operator, the RHS of Equation 2.3 is filled with elements  $B_{c,k}^{\mathbf{p}_x}$ . We will refer to this method of obtaining the weights as the *direct* method due to the ability to directly compute RBF-FD weights for operators  $\mathbf{P} \cdot \nabla \phi_k(r(\mathbf{x}))$  without the need to compute other weights.

## B.2 Indirect Weights

Alternatively, one could compute weights *indirectly* as a weighted combination of the weights for the unprojected  $\nabla$  operator.

Have not found in literature any mention of the fact that RBF-FD weights can be used to

first assembling differentiation matrices for the unprojected  $\nabla$  operator,

$$\mathbf{D}_\nabla = \begin{bmatrix} \mathbf{D}_{\frac{d}{dx}} \\ \mathbf{D}_{\frac{d}{dy}} \\ \mathbf{D}_{\frac{d}{dz}} \end{bmatrix}$$

where the matrices contain weights for the operators of Equation ??, and then apply the projection  $\mathbf{P}$  to the differentiation matrices:

$$\mathbf{P} \cdot \mathbf{D}_\nabla = \begin{bmatrix} \mathbf{D}_{\mathbf{p}_x \cdot \nabla} \\ \mathbf{D}_{\mathbf{p}_y \cdot \nabla} \\ \mathbf{D}_{\mathbf{p}_z \cdot \nabla} \end{bmatrix} = \begin{bmatrix} \text{diag}(1 - X^2) \mathbf{D}_{\frac{d}{dx}} - \text{diag}(XY) \mathbf{D}_{\frac{d}{dy}} - \text{diag}(XZ) \mathbf{D}_{\frac{d}{dz}} \\ -\text{diag}(XY) \mathbf{D}_{\frac{d}{dx}} + \text{diag}(1 - Y^2) \mathbf{D}_{\frac{d}{dy}} - \text{diag}(YZ) \mathbf{D}_{\frac{d}{dz}} \\ -\text{diag}(XZ) \mathbf{D}_{\frac{d}{dx}} - \text{diag}(YZ) \mathbf{D}_{\frac{d}{dy}} + \text{diag}(1 - Y^2) \mathbf{D}_{\frac{d}{dz}} \end{bmatrix} \quad (\text{B.4})$$

where  $X = \{x_{c,i}\}_{i=1}^N$ ,  $Y = \{y_{c,i}\}_{i=1}^N$ ,  $Z = \{z_{c,i}\}_{i=1}^N$  are all x-components, y-components and z-components of the stencil centers  $\{\mathbf{x}_{c,i}\}_{i=1}^N$  respectively.

In other words, we are able to compose differentiation matrices for complicated operators based on previously computed weights for the  $\nabla$

## B.3 Test Cases

We computed direct and indirect approaches for the following node sets:

```
'md010.00121'; 'md015.00256'; 'md019.00400'; 'md028.00841';
'md031.01024'; 'md049.02500'; 'md063.04096'; 'md079.06400';
'md089.08100' ; 'md100.10201' ; 'md127.16384' ; 'md165.27556'
```

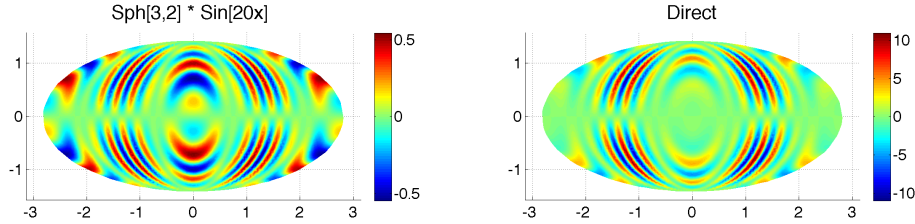
We check the relative error of the approximation:

$$\text{relative } \ell_2 \text{ error} = \frac{\|f_{\text{approx}} - f_{\text{exact}}\|_2}{\|f_{\text{exact}}\|_2}$$

We also look at the difference of relative errors and its absolute value:

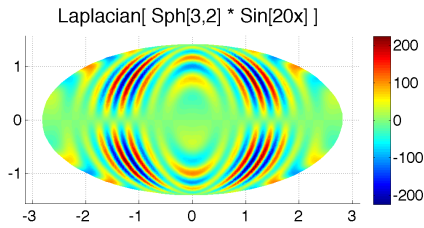
$$(\text{relative } \ell_2 \text{ error})_{\text{direct}} - (\text{relative } \ell_2 \text{ error})_{\text{indirect}}$$

We find that our indirect approach functions well compared to the direct method. For small node sizes ( $N < 2500$  nodes) we see that the direct method has the advantage with



(a) Manufactured test function:  
 $f(\mathbf{x}) = Y_3^2(\mathbf{x}) \sin(20x)$ .

(b)  $x$ -component of the projected gradient:  
 $\mathbf{p}_x \cdot \nabla f(\mathbf{x})$ .



(c) Surface Laplacian:  $\Delta_S f(\mathbf{x})$ .

Figure B.1: Test function and its projected  $x$  derivatives.

## B.4 Conclusions

Although it is clear the indirect method functions well compared to the direct method, we must consider its usefulness. Typically, weights are computed only as necessary for the PDE. If the PDE is on the sphere, then directly computing the  $\mathbf{P}\nabla$  operator would be most efficient for both memory and computation. However, one could imagine a scenario such as a 3-D spherical shell domain with physics on the boundaries that must be constrained to the surface, while the interior requires only an unprojected  $\nabla$  operator. In such cases, by simply computing for the  $\nabla$  operator, we assemble all necessary operators with minimal loss of accuracy and significant savings ( $3Nn$  doubles) in storage.

**Author's Note:** [Plot file size of matrix market file to give an idea of how much memory is saved by cutting out operators](#)

With  $N = 1e6$  nodes and stencil size  $n = 101$ , the matrix market file for weights is approximately 1.6 GB on disk. For a GPU with only 6 GB of global memory space available, it is worthwhile to consider possibilities for memory conservation.

**Author's Note:** [Check to see  \$\nabla \cdot \nabla\$  accuracy for heat equation.](#)

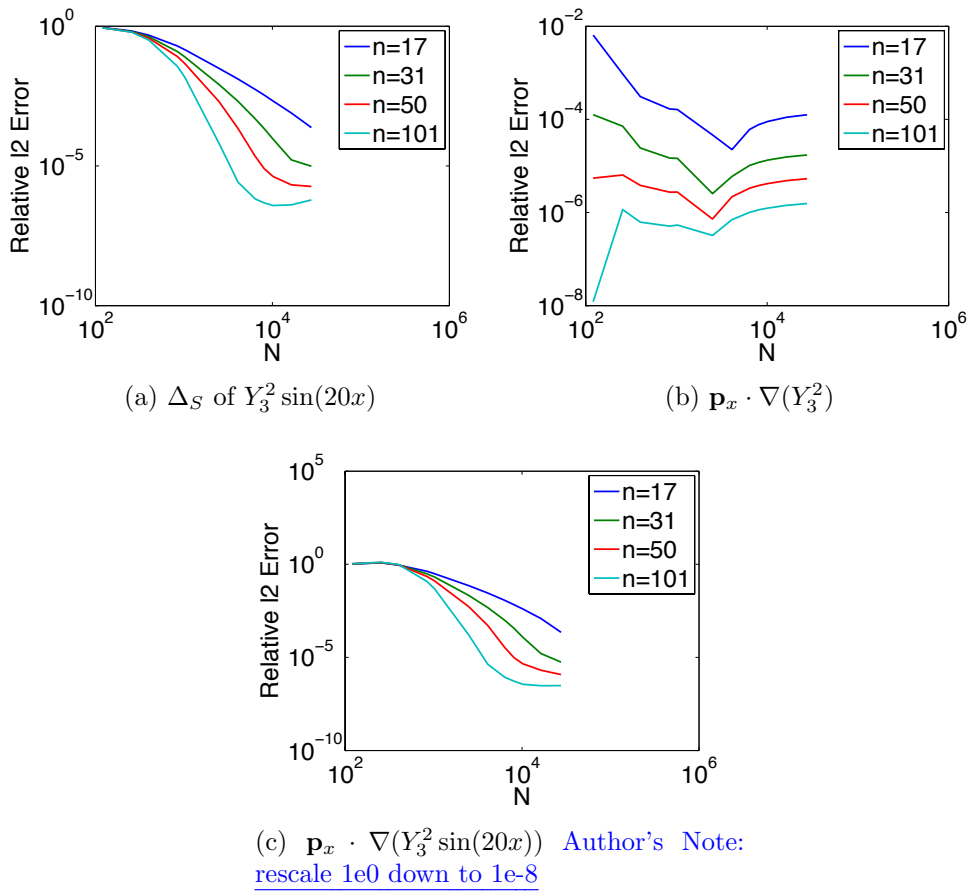


Figure B.2: Relative  $\ell_2$  error in differentiation.

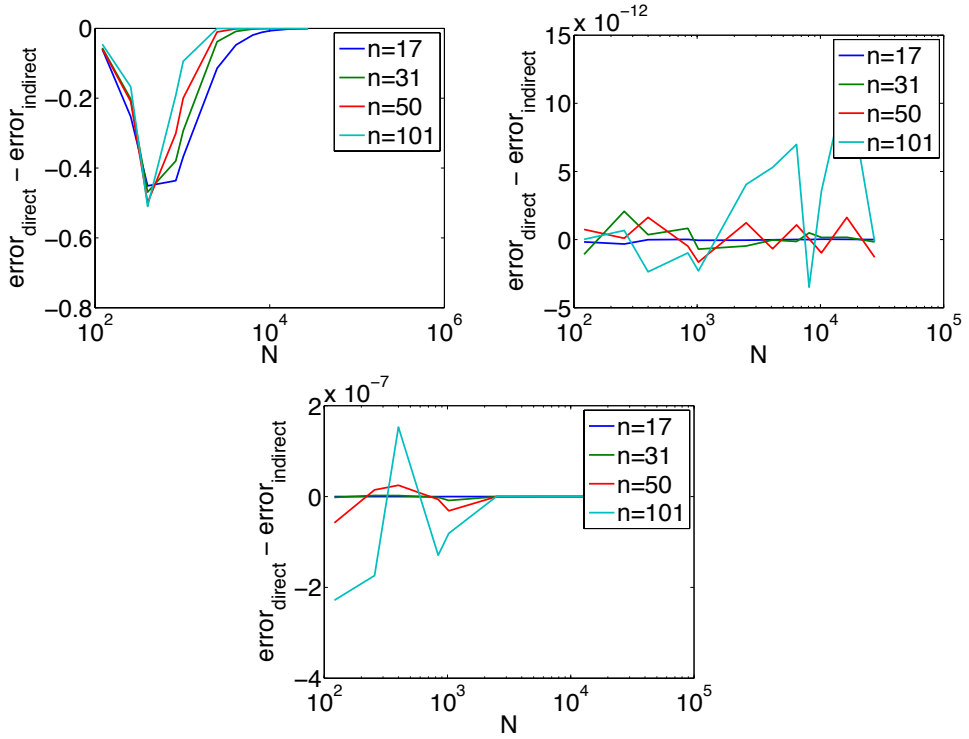


Figure B.3: Signed differences of relative  $\ell_2$  errors in differentiation between Direct and Indirect weights.

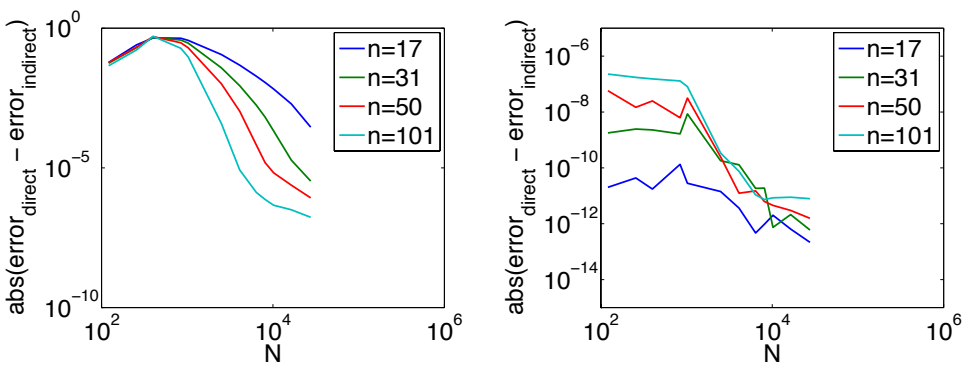


Figure B.4: Absolute differences of relative  $\ell_2$  errors in differentiation between Direct and Indirect weights.

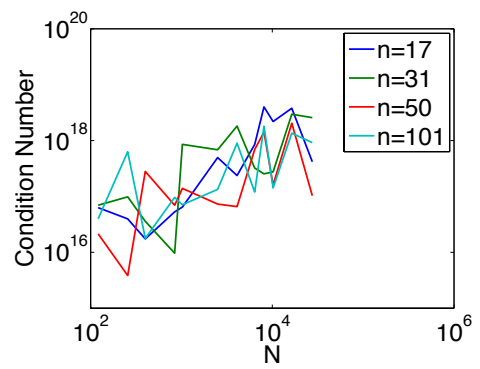


Figure B.5: Condition number estimates (condest) of direct  $\mathbf{p}_x \nabla$  differentiation matrix

## BIBLIOGRAPHY

- [1] HMPP Data Sheet. <http://www.caps-entreprise.com/upload/article/fichier/64fichier1.pdf>, 2009. [7](#)
- [2] AccelerEyes. *Jacket User Guide - The GPU Engine for MATLAB*, 1.2.1 edition, November 2009. [5](#)
- [3] Jacques M. Bahi, Raphaël Couturier, and Lilia Ziane Khodja. Parallel gmres implementation for solving sparse linear systems on gpu clusters. In Layne T. Watson, Gary W. Howell, William I. Thacker, and Steven Seidel, editors, *SpringSim (HPC)*, pages 12–19. SCS/ACM, 2011. [44](#), [45](#), [46](#)
- [4] Nathan Bell and Michael Garland. Implementing sparse matrix-vector multiplication on throughput-oriented processors. *Proceedings of the Conference on High Performance Computing Networking, Storage and Analysis - SC '09*, (1):1, 2009. [24](#), [45](#)
- [5] E. F. Bollig. A Multi-CPU/GPU implementation of RBF-generated finite differences for PDEs on a Sphere. Poster. American Geophys. Union. San Francisco, CA, December 2011.
- [6] E. F. Bollig. Accelerating RBF-FD in Parallel Environments. Student Presentation. NSF CBMS Workshop: Radial Basis Functions Mathematical Developments and Applications. Darmouth, MA, June 2011.
- [7] E. F. Bollig. Multi-GPU Solutions of Hyperbolic and Elliptic PDEs with RBF-FD. Contributed Talk. SIAMSEAS Annual Meeting. Huntsville, AL, March 2012.
- [8] E. F. Bollig. Parallel Algorithms for RBF-FD Solutions to PDEs on the Sphere. Poster. FSU Dept. of Sci. Comp. Computational Xpo. Tallahassee, FL, March 2012.
- [9] Evan F. Bollig. Fast neighbor queries and other optimization strategies for efficient radial basis function pde methods. *in preparation*, 2011. [10](#), [24](#), [42](#), [43](#)
- [10] Evan F. Bollig, Natasha Flyer, and Gordon Erlebacher. Solving Elliptic PDEs with RBF-generated Finite Differences on Multiple GPUs. *in preparation*, 2012.
- [11] Evan F. Bollig, Natasha Flyer, and Gordon Erlebacher. Using Radial Basis Function Finite Difference (RBF-FD) for PDE Solutions on the GPU. *in press. Elsevier J. Comput. Phys.*, 2012. [41](#), [43](#)

- [12] Andreas Brandstetter and Alessandro Artusi. Radial Basis Function Networks GPU Based Implementation. *IEEE Transaction on Neural Network*, 19(12):2150–2161, December 2008. 5
- [13] J. C. Carr, R. K. Beatson, B. C. McCallum, W. R. Fright, T. J. McLennan, and T. J. Mitchell. Smooth Surface Reconstruction from Noisy Range Data. In *GRAPHITE '03: Proceedings of the 1st international conference on Computer graphics and interactive techniques in Australasia and South East Asia*, pages 119–ff, New York, NY, USA, 2003. ACM. 5
- [14] Tom Cecil, Jianliang Qian, and Stanley Osher. Numerical Methods for High Dimensional Hamilton-Jacobi Equations Using Radial Basis Functions. *JOURNAL OF COMPUTATIONAL PHYSICS*, 196:327–347, 2004. 4, 5, 42
- [15] G Chandhini and Y Sanyasiraju. Local RBF-FD Solutions for Steady Convection-Diffusion Problems. *International Journal for Numerical Methods in Engineering*, 72(3), 2007. 3, 5, 42
- [16] P P Chinchapatnam, K Djidjeli, P B Nair, and M Tan. A compact RBF-FD based meshless method for the incompressible Navier–Stokes equations. *Proceedings of the Institution of Mechanical Engineers, Part M: Journal of Engineering for the Maritime Environment*, 223(3):275–290, March 2009. 5, 42
- [17] Michael Connor and Piyush Kumar. Fast construction of k-nearest neighbor graphs for point clouds. *IEEE Transactions on Visualization and Computer Graphics*, 16:599–608, 2010. 24
- [18] A Corrigan and HQ Dinh. Computing and Rendering Implicit Surfaces Composed of Radial Basis Functions on the GPU. *International Workshop on Volume Graphics*, 2005. 5
- [19] N Cuntz, M Leidl, TU Darmstadt, GA Kolb, CR Salama, M Böttinger, D Klimarechenzentrum, and G Hamburg. GPU-based Dynamic Flow Visualization for Climate Research Applications. *Proc. SimVis*, pages 371–384, 2007. 5
- [20] K Dekker. Parallel GMRES and Domain Decomposition. Technical report, Delft University of Technology, Delft, The Netherlands, 2000. 44
- [21] E Divo and AJ Kassab. An Efficient Localized Radial Basis Function Meshless Method for Fluid Flow and Conjugate Heat Transfer. *Journal of Heat Transfer*, 129:124, 2007. 5
- [22] Qiang Du, Vance Faber, and Max Gunzburger. Centroidal Voronoi Tessellations: Applications and Algorithms. *SIAM Rev.*, 41(4):637–676, 1999. 2
- [23] Qiang Du, Max Gunzburger, Lili Ju, and Xiaoqiang Wang. Centroidal Voronoi Tessellation Algorithms for Image Compression, Segmentation, and Multichannel Restoration. *Journal of Mathematical Imaging and Vision*, 24(2):177–194, 2006. 41

- [24] Gregory E. Fasshauer. *Meshfree Approximation Methods with MATLAB*, volume 6 of *Interdisciplinary Mathematical Sciences*. World Scientific Publishing Co. Pte. Ltd., 5 Toh Tuck Link, Singapore 596224, 2007. [2](#), [3](#), [4](#), [14](#)
- [25] Natasha Flyer and Bengt Fornberg. Radial basis functions: Developments and applications to planetary scale flows. *Computers & Fluids*, 46(1):23–32, July 2011. [4](#), [41](#)
- [26] Natasha Flyer and Erik Lehto. Rotational transport on a sphere: Local node refinement with radial basis functions. *Journal of Computational Physics*, 229(6):1954–1969, March 2010. [4](#), [27](#), [41](#)
- [27] Natasha Flyer, Erik Lehto, Sebastien Blaise, Grady B. Wright, and Amik St-Cyr. Rbf-generated finite differences for nonlinear transport on a sphere: shallow water simulations. *Submitted to Elsevier*, pages 1–29, 2011. [5](#), [9](#), [12](#), [13](#), [28](#), [42](#), [44](#), [50](#), [58](#)
- [28] Natasha Flyer and Grady B. Wright. Transport schemes on a sphere using radial basis functions. *Journal of Computational Physics*, 226(1):1059 – 1084, 2007. [4](#), [27](#), [30](#), [31](#), [33](#), [41](#), [56](#)
- [29] Natasha Flyer and Grady B. Wright. A Radial Basis Function Method for the Shallow Water Equations on a Sphere. In *Proc. R. Soc. A*, volume 465, pages 1949–1976, December 2009. [4](#), [12](#), [41](#), [50](#), [56](#), [57](#), [58](#)
- [30] B Fornberg, T Driscoll, G Wright, and R Charles. Observations on the behavior of radial basis function approximations near boundaries. *Computers & Mathematics with Applications*, 43(3-5):473–490, February 2002. [9](#), [44](#)
- [31] B. Fornberg and G. Wright. Stable computation of multiquadric interpolants for all values of the shape parameter. *Computers & Mathematics with Applications*, 48(5-6):853 – 867, 2004. [4](#)
- [32] Bengt Fornberg and Natasha Flyer. Accuracy of Radial Basis Function Interpolation and Derivative Approximations on 1-D Infinite Grids. *Adv. Comput. Math*, 23:5–20, 2005. [4](#)
- [33] Bengt Fornberg, Elisabeth Larsson, and Natasha Flyer. Stable Computations with Gaussian Radial Basis Functions. *SIAM J. on Scientific Computing*, 33(2):869—892, 2011. [4](#), [27](#)
- [34] Bengt Fornberg and Erik Lehto. Stabilization of RBF-generated finite difference methods for convective PDEs. *Journal of Computational Physics*, 230(6):2270–2285, March 2011. [5](#), [9](#), [13](#), [27](#), [31](#), [42](#), [44](#)
- [35] Bengt Fornberg and Cécile Piret. A Stable Algorithm for Flat Radial Basis Functions on a Sphere. *SIAM Journal on Scientific Computing*, 30(1):60–80, 2007. [4](#)
- [36] Bengt Fornberg and Cécile Piret. On Choosing a Radial Basis Function and a Shape Parameter when Solving a Convective PDE on a Sphere. *Journal of Computational Physics*, 227(5):2758 – 2780, 2008. [4](#), [27](#)

- [37] E. J. Fuselier and G. B. Wright. A High-Order Kernel Method for Diffusion and Reaction-Diffusion Equations on Surfaces. *ArXiv e-prints*, May 2012. [2](#)
- [38] D Göddeke, SHM Buijssen, H Wobker, and S Turek. GPU Acceleration of an Unmodified Parallel Finite Element Navier–Stokes Solver. *High Performance Computing and Simulation*, 2009. [43](#)
- [39] Prashant Goswami, Philipp Schlegel, Barbara Solenthaler, and Renato Pajarola. Interactive sph simulation and rendering on the gpu. In *Proceedings of the 2010 ACM SIGGRAPH/Eurographics Symposium on Computer Animation*, SCA ’10, pages 55–64, Aire-la-Ville, Switzerland, Switzerland, 2010. Eurographics Association. [11](#)
- [40] R Hardy. Multiquadratic Equations of Topography and Other Irregular Surfaces. *J. Geophysical Research*, (76):1–905, 1971. [3](#)
- [41] A. Iske. *Multiresolution Methods in Scattered Data Modeling*. Springer, 2004. [3, 4](#)
- [42] L. Ivan, H. De Sterck, S. A. Northrup, and C. P. T. Groth. Three-Dimensional MHD on Cubed-Sphere Grids: Parallel Solution-Adaptive Simulation Framework. In *20th AIAA CFD Conference*, number 3382, pages 1325–1342, 2011. [20](#)
- [43] R. Jakob-Chien, J.J. Hack, and D.L. Williamson. Spectral transform solutions to the shallow water test set. *Journal of Computational Physics*, 119(1):164–187, 1995. [27](#)
- [44] Masanori Kameyama, Akira Kageyama, and Tetsuya Sato. Multigrid-based simulation code for mantle convection in spherical shell using Yin–Yang grid. *Physics of the Earth and Planetary Interiors*, 171(1-4):19–32, December 2008. [41](#)
- [45] E J Kansa. Multiquadratics—A scattered data approximation scheme with applications to computational fluid-dynamics. I. Surface approximations and partial derivative estimates. *Computers Math. Applic.*, (19):127–145, 1990. [3, 6, 8, 41](#)
- [46] E J Kansa. Multiquadratics—A scattered data approximation scheme with applications to computational fluid-dynamics. II. Solutions to parabolic, hyperbolic and elliptic partial differential equations. *Computers Math. Applic.*, (19):147–161, 1990. [8](#)
- [47] George Karypis and Vipin Kumar. A fast and high quality multilevel scheme for partitioning irregular graphs. *SIAM Journal on Scientific Computing*, 20(1):359–392, 1999. [20](#)
- [48] Khronos OpenCL Working Group. *The OpenCL Specification (Version: 1.0.48)*, October 2009. [7, 17, 23, 26](#)
- [49] G Kosec and B Šarler. Solution of thermo-fluid problems by collocation with local pressure correction. *International Journal of Numerical Methods for Heat & Fluid Flow*, 18, 2008. [5](#)
- [50] Elisabeth Larsson and Bengt Fornberg. A Numerical Study of some Radial Basis Function based Solution Methods for Elliptic PDEs. *Comput. Math. Appl.*, 46:891–902, 2003. [4, 6](#)

- [51] Shaofan Li and Wing K. Liu. *Meshfree Particle Methods*. Springer Publishing Company, Incorporated, 2007. [2](#), [3](#)
- [52] Dave a. May and Louis Moresi. Preconditioned iterative methods for Stokes flow problems arising in computational geodynamics. *Physics of the Earth and Planetary Interiors*, 171(1-4):33–47, December 2008. [43](#)
- [53] Ramachandran D. Nair and Christiane Jablonowski. Moving Vortices on the Sphere: A Test Case for Horizontal Advection Problems. *Monthly Weather Review*, 136(2):699–711, February 2008. [27](#)
- [54] R.D. Nair, S.J. Thomas, and R.D. Loft. A discontinuous Galerkin transport scheme on the cubed sphere. *Monthly Weather Review*, 133(4):814–828, April 2005. [27](#), [30](#), [41](#)
- [55] NVidia. *NVIDIA CUDA - NVIDIA CUDA C - Programming Guide version 4.0*, March 2011. [6](#), [23](#), [24](#), [26](#)
- [56] Jia Pan and Dinesh Manocha. Fast GPU-based Locality Sensitive Hashing for K-Nearest Neighbor Computation. *Proceedings of the 19th ACM SIGSPATIAL GIS ’11*, 2011. [11](#)
- [57] Portland Group Inc. *CUDA Fortran Programming Guide and Reference*, 1.0 edition, November 2009. [7](#)
- [58] DA Randall, TD Ringler, and RP Heikes. Climate modeling with spherical geodesic grids. *Computing in Science & Engineering*, pages 32–41, 2002. [20](#), [41](#)
- [59] Karl Rupp, Florian Rudolf, and Josef Weinbub. ViennaCL-A High Level Linear Algebra Library for GPUs and Multi-Core CPUs. In *Proc. GPUScA*, pages 51–56, 2010. [44](#), [45](#)
- [60] Youcef Saad and Martin H. Schultz. GMRES: A generalized minimal residual algorithm for solving nonsymmetric linear systems. *SIAM J. Sci. Stat. Comput.*, 7(3):856–869, 1986. [45](#)
- [61] Yousef Saad. *Iterative Methods for Sparse Linear Systems*. Society for Industrial Mathematics, second edition, 2003. [17](#), [53](#)
- [62] C. Sanderson. Armadillo: An open source c++ linear algebra library for fast prototyping and computationally intensive experiments. Technical report, NICTA, 2010. [27](#)
- [63] Robert Schaback. Multivariate Interpolation and Approximation by Translates of a Basis Function. In C.K. Chui and L.L. Schumaker, editors, *Approximation Theory VIII–Vol. 1: Approximation and Interpolation*, pages 491–514. World Scientific Publishing Co., Inc, 1995. [4](#)
- [64] J. Schmidt, C. Piret, N. Zhang, B.J. Kadlec, D.A. Yuen, Y. Liu, G.B. Wright, and E. Sevre. Modeling of Tsunami Waves and Atmospheric Swirling Flows with Graphics Processing Unit (GPU) and Radial Basis Functions (RBF). *Concurrency and Computat.: Pract. Exper.*, 2009. [5](#), [42](#), [43](#)

- [65] C. Shu, H. Ding, and K. S. Yeo. Local radial basis function-based differential quadrature method and its application to solve two-dimensional incompressible Navier-Stokes equations. *Computer Methods in Applied Mechanics and Engineering*, 192(7-8):941 – 954, 2003. [4](#), [5](#), [42](#)
- [66] Ian H. Sloan and Robert S. Womersley. Extremal systems of points and numerical integration on the sphere. *Adv. Comput. Math.*, 21:107–125, 2003. [27](#), [33](#)
- [67] D Stevens, H Power, M Lees, and H Morvan. The use of PDE centres in the local RBF Hermitian method for 3D convective-diffusion problems. *Journal of Computational Physics*, 2009. [5](#), [42](#)
- [68] A. I. Tolstykh and D. A. Shirobokov. On using radial basis functions in a “finite difference mode” with applications to elasticity problems. In *Computational Mechanics*, volume 33, pages 68 – 79. Springer, December 2003. [4](#), [42](#)
- [69] A.I. Tolstykh. On using RBF-based differencing formulas for unstructured and mixed structured-unstructured grid calculations. In *Proceedings of the 16 IMACS World Congress, Lausanne*, pages 1–6, 2000. [4](#), [42](#)
- [70] J.S. Vetter, R. Glassbrook, J. Dongarra, K. Schwan, B. Loftis, S. McNally, J. Meredith, J. Rogers, P. Roth, K. Spafford, and S. Yalamanchili. Keeneland: Bringing heterogeneous GPU computing to the computational science community. *IEEE Computing in Science and Engineering*, 13(5):90–95, 2011. [7](#)
- [71] M Weiler, R Botchen, S Stegmaier, T Ertl, J Huang, Y Jang, DS Ebert, and KP Gaither. Hardware-Assisted Feature Analysis and Visualization of Procedurally Encoded Multifield Volumetric Data. *IEEE Computer Graphics and Applications*, 25(5):72–81, 2005. [5](#)
- [72] Holger Wendland. Piecewise polynomial, positive definite and compactly supported radial functions of minimal degree. *Advances in Computational Mathematics*, 4:389–396, 1995. 10.1007/BF02123482. [4](#)
- [73] Grady B. Wright. *Radial Basis Function Interpolation: Numerical and Analytical Developments*. PhD thesis, University of Colorado, 2003. [4](#), [42](#)
- [74] Grady B. Wright, Natasha Flyer, and David A. Yuen. A hybrid radial basis function–pseudospectral method for thermal convection in a 3-d spherical shell. *Geochem. Geophys. Geosyst.*, 11(Q07003):18 pp., 2010. [4](#), [11](#), [41](#), [49](#)
- [75] Grady B. Wright and Bengt Fornberg. Scattered node compact finite difference-type formulas generated from radial basis functions. *J. Comput. Phys.*, 212(1):99–123, 2006. [8](#), [9](#), [44](#)
- [76] Rio Yokota, L.A. Barba, and Matthew G. Knepley. PetRBF — A parallel O(N) algorithm for radial basis function interpolation with Gaussians. *Computer Methods in Applied Mechanics and Engineering*, 199(25-28):1793–1804, May 2010. [5](#), [43](#), [44](#)